Discrete Fracture Network Model for Numerical Analysis of Tight Unconventional Reservoirs

by

Pedro Abdiel Mateo Villanueva

A thesis submitted in partial fulfillment of the requirements for the degree of

Master of Science
in
Petroleum Engineering

Department of Civil and Environmental Engineering

University of Alberta

Abstract

Fracking, or hydraulic fracturing, is a process where high permeability fractures are induced in low permeability reservoir rocks in order to create a more conductive pathway for oil production. Production from shale and other low permeability reservoirs is a complex multi-physics problem. The interaction between the natural fractures already present in the formation and the fractures induced from the fracking process, coupled with the uncertain spatial distribution of the heterogeneous features, introduce even more uncertainty to the production estimates. Numerical modelling of tight and shale formations is, for this reason, still challenging.

Various numerical methods have been used to study flow and immiscible displacement through fractured reservoirs. While all numerical methods make compromises due to the highly complex nature of oil reservoirs, the discrete fracture (DF) method based on the Mixed Finite Element (MFE) discretization scheme proves to be a superior alternative for computational analysis of fractured media. While the numerical accuracy of the three most common schemes to study transport in oil formation; the finite difference (FD), finite element (FE), and finite volume (FV) method, strongly rely on the grid size of the matrix cells, the MFE formulation can be frame din such a way to relax this dependency. Additionally, while local mass continuity cannot be ensured in the conventional finite element method, it is naturally incorporated in the mixed finite element formulation. A novel modelling framework is proposed where point-source well models are incorporated in order to simulate production from tight reservoirs with natural and hydraulic fractures. To eliminate the need for local grid refinement when implementing the discrete fracture model, both natural and hydraulic fractures are represented physically as lower-dimensional features in the numerical

domain, making our method a computationally efficient approach.

The proposed model is suitable to account for reservoir heterogeneities and is also able to handle irregular reservoir geometries and arbitrary fracture orientation; which are some of the major drawback of many existing numerical algorithms used to study tight reservoirs. We Modelled single phase flow moving inside a fractured reservoir, using the Discrete Fracture Network approach where fractures are represented by lower dimensional spatial features in the computational domain to avoid grid refinement. The model introduced a point source well model based on Darcy's law applied inside the fracture network. The results of this thesis demonstrated that model accuracy of the MFE-based numerical scheme is achieved using a much lower mesh density when comparing to conventional Finite Elements-based commercial software. Additionally, the developed model, coupled with the point source well model predicted very similar production profiles to popular reservoir simulators, assuming orthogonal fractures. When studying non-orthogonal fractures the model indicated that uniformly distributed, well connected fracture networks will impact positively the oil production, and that for the cases where the hydraulic fractures are well connected, regardless of fracture orientation, the fracture pressure is almost constant.

Although the MFE formulation has been implemented to model fractured reservoirs in the past, an implementation used to study the production/extraction process from unconventional formations by means of a well model using a natural MFE scheme is novel.

Keywords: Tight reservoirs, discrete fracture network, mixed finite elements, porous media flow, computational fluid dynamics

Dedicated to my dear family, and my dear little boy.

Acknowledgements

I would like to thank my family, for their unconditional love and support during my studies. I would also like to thank Maria for giving me the blessing to be a dad during the culmination of my studies. I would like to thank my supervisor, for her guidance and patience, and the members of my research group for their kind words and encouragement. I would like to thank my dear friends, who went beyond friendship and cultivated bonds that will last a lifetime.

I would like to thank COMSOL Multiphysics, Computing Modelling Group, and Silverfrost for providing academic licenses for COMSOL Multiphysics, CMG IMEX, and Silverfrost FTN95.

Table of Contents

List of Tables

List of Figures

Chapter 1

Introduction

In this chapter, I briefly describe the origin of the problem we are studying, and explain our motivation to complete this work. Additionally, we clearly presents the contributions of this thesis, and present the structure of this document per chapter.

1.1 Shale Formations and The Fracking Process for Unconventional Oil Recovery

Shale formations are believed to be formed around 300 million years ago, via deposition of fine silt and clay particles in enclosed bodies of water [1]. Organic matter trapped inside these low permeability layers became what we know today as shale gas and shale oil. Tight oil was formed around the same time, but by different mechanisms. Both shale and tight oil are considered unconventional oil resources.

Some of these unconventional formations confine large amounts of petroleum and natural gas. The US Department of Energy, the unproved recoverable shale gas in the United States of America is estimated at around 482 trillion cubic feet, and the estimated proved and unproved shale gas reserves is estimated at around 542 trillion cubic feet [1, 2]. In Canada, the average daily production from shale gas was estimated at 2 billion cubic feet in the year 2012, helping to establish North America as the world's largest production of shale gas [3].

Fracking, or hydraulic fracturing, is a production stimulation technique where mechanical and chemical enhancement of the rock/fluid interactions is achieved by injecting a pressurized fluid into the extraordinary impermeable formation in order to create high permeability conduits (fractures) in an otherwise low or ultra-low permeability reservoir, as explained by King and Durham [4]. Via this process, oil production from shale formations and other geological formation with low and ultra-low permeability and porosity can be enhanced

Fracking technology became popular due to the large amounts of natural resources trapped inside geological formations with very low permeability. Early predictions stated

that by the year 2035, approximately 13.6 trillion cubic feet of oil per year will be produced from shale formations; representing around 49 percent of the total U.S. dry gas production [2]. Therefore, fracking will continue to have an important role on some of the most powerful economies in the world.

With numerous instances of successful implementation of fracking low permeability formations in North America, this process has proven to be a very effective technique. However, issues that are related to fracturing and should be optimized include:

- Water utilization. A single well may require up to 10 million gallons of water to perform hydraulic fracturing, which can be an issue especially in places where water is not an abundant resource [5, 6].
- Groundwater contamination. Whether the contamination originates from the fracking fluid breaking the rock and reaching underground aquifers, of by oil spills at the surface level, the impact and risks of fracking remain a controversial topic [5, 7].
- Seismic activity. Although the U.S. Department of Energy reported that the energy released to subsurface geomorphology is not large enough to trigger seismic activity that could be felt in the surface, induced seismic events are often attributed to the fracking process and thus require additional research [5, 8].

Thus, the fracking process and production from fractured, horizontal wells are still full of unexplored areas. Further studies related to fracture spacing and fracture connectivity optimization could lead to a significant reduction of utilized water, thus decreasing the changes of underground water contamination and fracking induced seismic activity. For this, we need to improve our current numerical models.

1.2 Motivation

As indicated by the U.S. Department of Energy [1] and the Canadian Office of the Parliament [3], North America is a region rich in unconventional resources. Their proper exploitation could lead to great revenue and a shift on the economies of the two countries. Worldwide, shale gas production may be one of the keys to extend the life of fossil fuels as an accessible energy source.

To better design the fracking process, the transport mechanisms and the rock-fluid interactions, numerical models are the key. Due to the scales of these geological formations, lab studies and other performance prediction tools are not suitable when accuracy is important, thus lab scale models are generally not the best alternative to study fracking and production.

Furthermore, even numerical models face difficulties when we look at the fracking process. Fracking a horizontal well generally consists on more than one fracking stage, thus the connecting surface between matrix and fracture of each stage plays a fundamental role on oil production. Additionally, the difference in spatial scales (horizontal wells are in the meter to centimetre scale in diameter but in between the hundred-meter scale and the kilometre scale in length, fractures are well within the centimetre scale, fracking stages are in the hundred metre scale, and the complete formation is usually in the kilometre scale), the correct modelling approach remains a debatable topic. To handle wells, well models are popular alternatives [9]

Moreover, in addition to all the characteristics previously mentioned, sub-surface formations are generally heterogeneous, and natural discontinuities (natural fractures that occur inside the shale formations, which were not created by the fracking process and rather by the deposition mechanism of the silt and clay that created the formations hundred of million years ago, as well as natural seismic movement) may also interact with the production process from a fractured reservoir. Additionally, these natural occurring fractures may not have the same spatial scale or distribution than the hydraulic fractures, which while not orthogonal but are often oriented on a similar irregular pattern.

Studying the different ways in which fracture networks can be represented and modelled, leading then to a more accurate oil production model, would provide a solid first-step in the process of creating the next generation computer models and frameworks of study for fractured reservoirs with irregular fracture distributions.

Numerous existing modelling schemes and simulation packages exist, but they all have deficiencies that could be solved by implementing a different modelling approach. Generalist commercial packages based on the conventional finite element method such as COMSOL [10] can be used to model fractured reservoir, but they require extensive grid refinement to accommodate the fractures due to their spatial scale. Commercial packages such as CMG [11, 12] can be used to model fractured reservoirs as well, but they require fractures to be of orthogonal orientation and this assumption is unrealistic due to the irregular, tortuous nature of the fractures obtained when performing hydraulic fracturing. Software such as Intersect [13] can be used to model complex fracture networks, but higher order numerical solution schemes could be implemented. Individual researchers have developed numerical schemes to study fractured reservoirs as well [14, 15], but due to the use of control-volume approaches and the necessity to use two point or multi point flux approximations, results may not be locally conservative for fluxes and velocity fields.

In addition, popular schemes used to model subsurface flow such the the conventional Finite Element Method, the Control Volume Finite Difference and Control Volume Finite Element can't ensure local mass conservation due to the irregular domains being used.

Previously, advanced modelling formulations have been implemented in the form of the Mixed Finite Element Method (MFE), but they were not focused on unconventional oil production, they focused on immiscible displacement of oil by water; with notable contributions made by Hoteit and Firoozabadi [16, 17]. This thesis takes the methodology documented by Hoteit and Firoozabadi [16] and Hoteit and Firoozabadi [17], simplified the MFE formulation to a more natural discretization scheme where the solution variables are pressure and velocities instead of just pressures, and incorporates a point source well model. The MFE method has the conventional mesh flexibility of the conventional finite element method, and also adds local mass conservation. This makes the MFE method a more accurate numerical scheme in terms of flow pattern predictions than all numerical schemes previously discussed in this section.

1.3 Contributions

In this thesis we present a methodology to model single phase flow through fractured, unconventional, slightly compressible reservoirs with well models to study oil production. While The MFE scheme was already proven to be an effective way to include fractures as heterogeneities in DFN models. For this work, we extended the MFE implementation to simulate production from a single fracking plane presenting different fracture configurations; thus creating a model which is able to handle heterogeneities, flexibility to be used in DFN formulations, and is both locally and globally mass conservative. For the test cases evaluated, we assumed homogeneous effective transport properties, and confirmed the validity of the MFE formulation using a commercial FEM package and a commercial black oil reservoir simulation package. We use a sequential validation approach, where we validate first the MFE solver, then the integration of the fracture network, and finally the point source well models.

The novelty of this thesis is that we couple one of the most robust numerical schemes used to model flow through porous media and fractures at different spatial scales with a simple yet effective well model in order to study the transport mechanism of hydraulic fractures at different orientations. The foundations for this thesis started with the work done by Hoteit and Firoozabadi [17] and Hoteit and Firoozabadi [16], where a more conventional formulation of the MFE method was used, and a well model was added to study the production process rather than immiscible displacement. The main contributions of this thesis are:

- A model based on the conventional Mixed Finite Element method, where flow potential is evaluated at the center of the elements and fluxes or velocities are evaluated at the edges of the elements.

- Incorporation of a well model to study the transport mechanism of hydraulic fractures in unconventional reservoirs, and the ability to directly compare the obtained results with well established simulation packages.
- A methodology to build irregular domains that contain natural and hydraulic fractures based on mesh generation techniques created for the Finite Element Method.

1.4 Structure of the Thesis

This documents presents a framework to study unsteady, single-phase flow through subsurface geological formations with ultra-low permeability and with natural and hydraulic fractures. The basic concept of fracking, the motivation for this project, and the main contributions of this thesis are presented in Chapter 1. The literature review regarding the different methods used to model fractured porous media and the different numerical schemes and numerical solution approach are all presented in Chapter 2. The governing equations, proposed well production model, and numerical discretization of our proposed modelling framework using the Mixed Finite Element Method is presented in Chapter 3. Results from our validation studies, and selected implementation to quantify the applicability of our proposed model is presented in Chapter 4. Finally, Chapter 5 presents our final remarks, contributions, and directions for future work.

Chapter 2

Literature Review

2.1 Numerical Schemes for Simulation of Flow in Unconventional Reservoirs

Fractures exist in nature, and are relevant in a variety of scenarios, all relevant to the scientific community. Geology and geomorphology, unconventional oil and gas reservoirs, human physiology, and design of solid structures such as buildings, water dams and nuclear reactors are just some examples of how fractures interact with other physical phenomena. Mechanically inducing fractures on low permeability reservoirs has increased their exploitation and overall economical feasibility, and thus accurate modelling of fractured media is imperative, and as stated by Narr et al. [18], all reservoirs should be considered fractured unless there is certainty about the absence of such spatial heterogeneities. Over recent years, research about modelling and discretization of discrete fracture networks has increased significantly, and open source solutions such as the Alghalandis discrete fracture network engineering package [19], which specialized on fracture discretization and statistical properties of fracture networks; and the Matlab Reservoir Simulation Toolbox (MRST), developed and documented by Krogstad et al. [15], which is a general purpose framework for black oil and compositional reservoir simulation, have arisen. Yet, modelling fractured media remains a demanding, complex task. Although, current research is rapidly improving and correcting the present limitations for discrete fracture modelling on unconventional reservoirs.

All computational studies of fracture network in unconventional reservoirs can be grouped into three main categories, as presented by Hoteit and Firoozabadi [17] and references therein: single porosity models, dual porosity models, and discrete fracture network models. Regardless of the modelling approach, all reservoir simulations are based on either the finite difference method, the finite element method, control volume methods, and more recently the mixed finite element method.

The Finite Difference Method is very popular for sub-surface flow researchers due to

its simplicity, and easy incorporation with other techniques widely used in the oil and gas industry such as streamline simulations and inclusion of PVT properties. Yan et al. [20] developed a mimetic finite difference method to study DFN on structured grids, and since fractures are represented by lines in a 2-dimensional domain the model is easy to implement, very computationally efficient, and has the capability to easily representing very complex fracture networks; but due to the utilization of an orthogonal grid, fractures at an arbitrary angle are not represented by this model. Zhang et al. [21] took the concept of mimetic finite difference schemes further to represent field-scale problems by the incorporation of multiscale modelling, where the interactions between the matrix and fractures is captured by multi-scale basis functions which are obtained from the mimetic finite difference method on a local fine grid, and multiple fine-scale grids form a coarse grid cell. Although the finite difference scheme can be used with irregular grids as shown by Liu and Yuan [22], Zingg and Lomax [23], most of the work on this area is done with orthogonal, regular domains with the aid of grid refinement when needed. Higher order finite difference schemes have also been implemented, for instance by Li and Yuan [24] and Douglas et al. [25] respectively; but while all these schemes are generally robust and computationally efficient, their implementation on only orthogonal grids severely hinders their applicability. The simulation package offered by CMG [11], is a commercial reservoir simulation suite based on the finite difference scheme capable of modelling natural and hydraulic fractures using the single porosity simulation approach; but its utilization to study unconventional reservoirs is limited to geometries meshed using orthogonal grids; thus becomes impossible to model fracture at an arbitrary orientation.

The Finite Element Method is a powerful numerical scheme to solve multi-physics problems, particularly suited for irregular computational domains as stated by Bramble and Zlámal [26], Zienkiewicz et al. [27]. With a more complex mathematical background, the FEM has been successfully implemented to study oil and gas flow on reservoirs and fractured porous media, as reported by Jiang and Dahi Taleghani [28], Chavent and Jaffre [29, 30], Noorishad and Mehran [31], and references therein. Commercial software solutions based on the finite element method such as COMSOL [10] have been used to model fractured reservoirs as documented by Yan et al. [32], Mi et al. [33]. The FEM is suitable for DFN implementation; however, as pointed out by Durlofsky [34], Klausen and Russell [35], the conventional finite element method is not locally mass conservative and therefore post-processing techniques are usually required to guide the results to satisfy local mass conservation across the element faces.

The Control Volume Finite Difference and Control Volume Finite Element methods combine the local mass conservation from the Control Volume formulation, but add flexibility of allocating triangular domains to model flow through porous media and discrete fracture

networks [36–41]. While certainly allowing the implementation of a model using the DFN approach, the control volume based schemes such as the CVFD rely on Two-Point Flux Approximation (TPFA) or Multi-Point Flux Approximation (MPFA) [40, 42, 43], to estimate the fluxes based on the pressures of the control volumes, hindering accuracy of the models and thus having a linked dependency between grid orientation and the validity of the results. Some of the well known issues with CVFE schemes is the fact that they may become invalid when the capillary pressure at the fractures is zero, as referred by Hoteit and Firoozabadi [17]. Additionally, since some discrete fracture network numerical models with control volume-based schemes rely on averaging matrix and fracture properties on a control volume, the difference of length scales (centimetre scale for fractures, kilometre scale for the matrix) may cause unrealistic flow between matrix and fracture cells.

A promising alternative for modelling subsurface flow came along in the form of the mixed finite element method. While keeping the strengths of the conventional Galerkin finite element method, the Mixed Finite Element method is by definition also locally mass conservative, as explained by Klausen and Russell [35], Brezzi and Fortin [44], Brezzi et al. [45], Raviart and Thomas [46], A. Raviart and M. Thomas [47], Liu et al. [48] and references therein. Although the mixed finite element method has not been implemented on commercial modelling solutions for subsurface flow through porous and fractured media, the coupling between DFN and MFE emerges as a very strong candidate for accurate flow modelling for unconventional tight reservoirs; being locally conservative, computationally efficient, and suitable for the modelling of irregular, heterogeneous porous media even with nonconforming grids, as previously demonstrated by Hoteit and Firoozabadi [16, 17], Vohralík et al. [49], Frih et al. [50], Masud and Hughes [51], Hughes et al. [52], Hoteit and Firoozabadi [53, 54], Fučík and Mikyška [55], Hoteit and Firoozabadi [56], Maryška et al. [57, 58], Vohralík et al. [59].

2.2 Single Porosity Models

Regardless of the solution method and implemented numerical schemes, single porosity models (SPM) are often viewed as the modelling benchmark. These models represent fractures explicitly in the computational domain, so the whole reservoir is represented as a continuum model. Tomin and Pergament [60] presented a single porosity model for two-phase flow through porous media with high conductivity fractures; based on capillary equilibrium and to account for the different scales and general anisotropy of two phase flow through fractured reservoir systems grid refined was required to produce adequate results. Abdel-Ghani [61] created pseudo-relative permeability curves for oil-water systems to account for the higher conductivity of fractures without modifying the computational domain, thus relaxing the necessity of grid refining but now requiring an accurate way to represent the pseudo relative

permeability curves to allow water and oil to interact as observed in field and laboratory settings. Ghorayeb and Firoozabadi [62] generated a SPM to study a single-phase, dual component fluid flow scenario under a linear temperature variation profile in order top look at the effects of temperature and fracture parameters such as aperture and connectivity on fluid compositional variation. While having a very strong link with the physics that take place in subsurface flow, single porosity model have the drawback of being generally a complex example of heterogeneous reservoir where the matrix and fractures are meshed equally on the domain and thus complex geometries involving the fracture network; the different scales between matrix reservoir; hydraulic fractures, and natural fractures; and fracture orientation can make these models very difficult to formulate and solve numerically. Since natural fractures and hydraulic fractures have very distinct origins, their dimensional scales will likely be very different; thus not only the difference of scales between fractures and reservoirs is important, but also the possible difference of scales within fractures plays an important role on the modelling criteria, and adds an extra layer of complexity.

2.3 Dual Porosity Models

Dual porosity models (DPM) are numerical schemes in which the matrix and fractures are two networks which overlap in the computational domain, and the interaction between matrix and fractures is captured by transfer functions which are empirically obtained, as indicated by Barenblatt et al. [63]. Doe et al. [64] provided one of the first examples of DPM on numerical simulations of fractured reservoirs, where matrix-fracture interactions were represented by a matrix storage element associated with each fracture, but the level of integrity of the proposed simulation methodology relied on the selection of adequate storage element size and shape. Warren and Root [65] provided initial analytical solutions for naturally fractured reservoirs but did not include source terms to study the production process. Arbogast [66] developed an analytical solution for incompressible, immiscible flow through naturally fractured porous media using the dual porosity approach; but while it allows the incorporation of combined Dirichlet and Neumann boundary conditions in order to potentially define well models, this work did not focus on unconventional, ultra low permeability rock formation with hydraulic fractures. Bai et al. [67] introduced a non-linear dual porosity single-phase model in which the flow potential for matrix and fractures is decoupled and solved individually by assuming quasi-steady state flow through the matrix, but such assumption will not hold true for ultra low permeability reservoirs with high conductivity hydraulic fractures, particularly for early production dates. Presho et al. [68] used the DPM for single-phase tracer flow modelling through fractured reservoirs and studied the different shape factors which can be used to fully formulate the models and transfer functions between matrix and

fractures, but appropriate selection of shape factors continued to affect the numerical results. Guo et al. [69] used dual porosity models to study gas sequestration inside permeable, fractured media assuming buoyant segregation under unsteady, two-phase flow conditions; where the fracture domain was formulated to reduce one modelling dimension due to vertical segregation, thus simplifying the model from fully 3D to 2D. The common issue of all DPMs is that their accuracy depends on the quality of the transfer functions and their ability to capture the matrix-fracture interactions precisely, and this issue becomes even more critical for multi-phase, multi-component flow as further explained by Hoteit and Firoozabadi [17], Lim and Aziz [70]. Gong and Rossen [71] reported on a methodology to study shape factors between matrix and fractures and concluded that fractures that are not well connected or fracture networks that have a wide range of aperture values do not contribute to the flow pattern of fractures reservoirs and that instead shape factors should be selected based on the fracture sub-domain which carries most of the injected fluid for enhanced oil recovery scenarios. Similarly, Douglas et al. [25] studied water flooding under incompressible, two-phase, immiscible conditions for naturally fractured reservoirs using a finite difference scheme and demonstrated that accuracy of the results is related to the gridblock size. Zimmerman et al. [72] eliminated the need to grid matrix gridblock for two-phase flow by using average values of pressure, saturation and other thermodynamic properties and incorporating them as source terms for the fracture cells, which due to the high conductivity are more relevant, but the approach did not extend to ultra-low permeability scenarios where capillary pressure may be discontinuous between matrix and fracture cells. Wu and Pruess [73] proposed an extension to the dual porosity model in which flow between matrix and fracture is assumed to be transient, and while not as computationally efficient as the steady or quasi-steady flow between matrix and fractures, the approach proved to be superior thus revealing the need of more complex modelling mechanism for the transfer functions beyond the solution space of gradients between matrix and fractures.

2.4 Discrete Fracture Models

The last category of fractured media models are known as Discrete fracture network (DFN) models. DFNs are a simplification of single porosity models, where fractures are represented as a lower dimension for the meshing process, but still explicitly taken into consideration during the mathematical formulation modelling process. Noorishad and Mehran [31] compared one and two dimensional analytical solutions with a discrete fracture model using the finite element method, but the validation studies were performed in a centimetre scale, where the magnitude and dimensionality of the fracture networks do not correspond to those observed in field scale production from unconventional reservoirs. Also based on a finite element

technique, Baca et al. [74] developed a DFN model based on the superposition of separate matrix and fracture networks, but well models and the oil production process were not in the scope of this study. More recently, Sandve et al. [40] used a control volume modelling approach coupled with the multi-point flux approximation, which proved superior to results from similar modelling approaches using a simple version of the two-point flux approximation for two-dimensional simulations. Haegland et al. [75] also used the MPFA approach, but compared the cell centred control volume approach with equi-dimensional fractures with the vertex-centred control volume approach with lower dimensional fractures and concluded that lower-dimensional representation of the fractures is justifiable numerically only when the fractures are highly permeable. The two-point flux approximation has also been successfully implemented with higher order schemes, such as the Control Volume Finite Difference formulation developed by Karimi-Fard et al. [76]. Mustapha et al. [77] designed a meshing algorithm for DFN models in three-dimensions, where fractures were represented by two-dimensional inclined planes and demonstrated the ability of representing complex fracture geometries with computationally efficient three-dimensional domains. Other control-volume based methods have been implemented by Monteagudo and Firoozabadi [37, 38, 39], where approaches such as cross-flow equilibrium between matrix and fractures, and reservoir wettability; and averaging techniques to represent the high degree of reservoir heterogeneity encountered in field applications. Hoteit and Firoozabadi [17] introduced a variation of the mixed finite element method in which the solution variables are the matrix and fracture flow potentials to formulate and solve two-phase flow through fractured porous media, reducing the numerical dispersion and convergence rates for unstructured meshes, but considering immiscible displacement only and well models and oil production were not included. DFN models are attractive because they are completely based on the subsurface physics governing the flow; the fact that fractures are represented in a *(n-1)-D* dimensions for an *n-D* computational domain, thus removing the requirement for extensive grid refinement to represent even the smallest of features, and therefore being nearly as computationally efficient as DPM schemes.

However, DNF schemes also have many challenges for accurately describing unconventional reservoirs with natural and hydraulic fractures. With fractures being represented as lower dimensional features int he physical domain, information about thickness variability is lost in the formulation. The Finite Difference (FD), Finite Element Method (FEM), Control Volume Finite Difference (CVFD), Control Volume Finite Element (CVFE), and the Mixed Finite Element (MFE) method are some of the schemes that have been successfully implemented using the DFM approach.

2.5 Generating the Computational Domain

Multiphysics problems for subsurface flow are often too complex to be represented by analytical solutions. Thus, dividing the spatial domain we want to study into many, smaller sub-domains and then discretizing the governing equations to solve them inside each of the created sub-domains is often the path taken by researchers and scientists.

These sub-domains take often the form of primitive geometric figures, such as tetrahedra in three-dimensional spaces and triangles in two dimensional spaces. The process and results from dividing the physical domain into smaller sub-domains is known as computational mesh generation, and the process in which governing equations are discretized and solved inside these sub-domains is known as Computational Fluid Dynamics (CFD).

A mesh can be structured, unstructured, and hybrid/non conforming. In a structured mesh [78, 79], the main characteristic feature is the regular connectivity of the elements, where the elements are regularly oriented in a orthogonal fashion, as shown in Figure 2.1. Structure meshes are very computationally efficient, but their orthogonality hinders the complexity of geometries that can be modelled. Finite difference schemes and control-volume based schemes can be easily coupled with structured meshes.

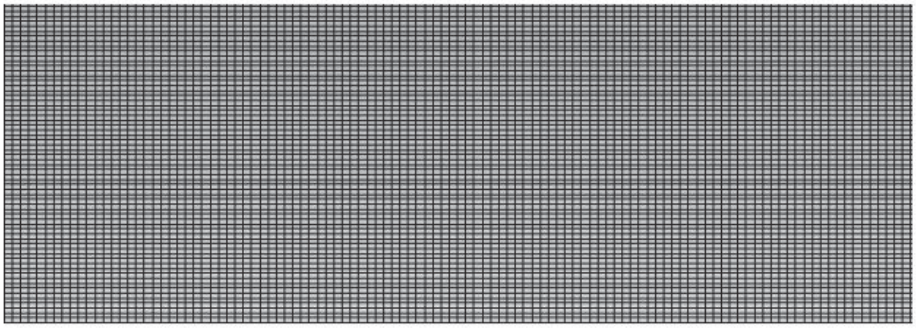

Figure 2.1 – Structured mesh with quadrilateral elements.

An unstructured mesh [78–81] is characterized by an irregular connectivity of the elements. Since their connectivity is not limited to orthogonal directions, virtually any geometry can be decomposed using unstructured meshes. These meshes are very suitable for control volume schemes and finite element-based schemes. The main downside of unstructured meshes is that they require additional (sometimes substantial) storage because of the irregular element interconnectivity, which means that information about a discrete element and it's interaction with other elements must be stored. A typical unstructured mesh is presented in Figure 2.2.

The Perpendicular Bisector (PEBI) grids are also a popular variation of unstructured grids used for reservoir simulations [82–84] where the mesh is created by placing points

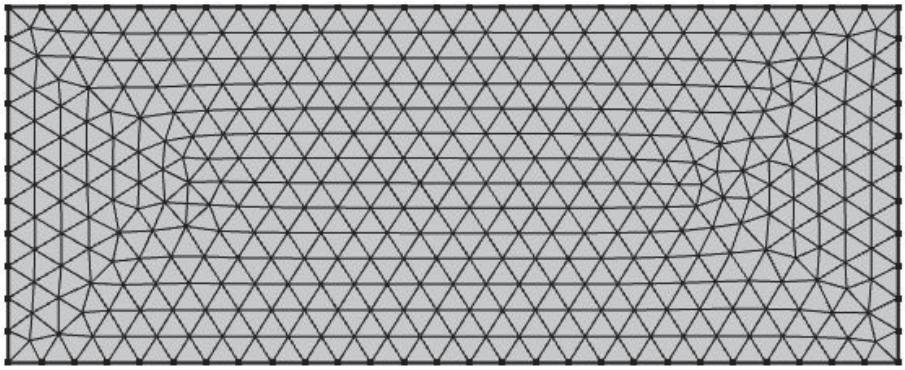

Figure 2.2 – Unstructured mesh with triangular elements.

around the geometry of the desired domain, and then creating cells by creating perpendicular bisection lines between these points in space. Grid refinement is naturally taken into account by controlling the spacing between the points before creating the bisection planes.

A hybrid mesh [79, 85–87] is a discretization scheme where particular spatial regions are discretized using different meshing geometries. A hybrid mesh could be a combination of structured and unstructured meshes, but could also be a combination of two distinct unstructured meshes as well (such as triangular and irregular quadrilateral elements). A simple hybrid mesh with structured and unstructured elements is presented in Figure 2.3.

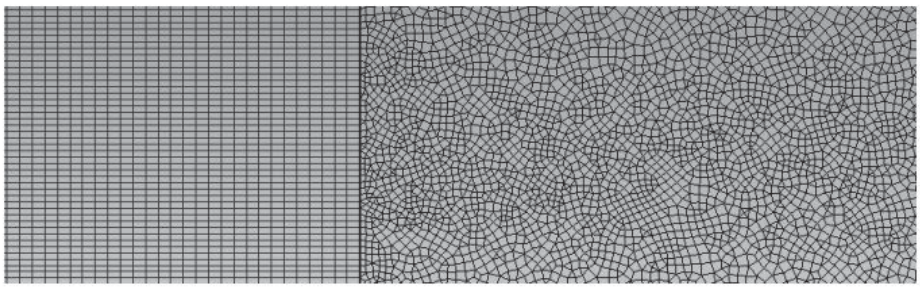

Figure 2.3 – Hybrid mesh, with a combination of structured quadrilateral elements and unstructured quadrilateral elements.

Chapter 3

Discrete Fracture Network Model

In this chapter, we formulate the governing equation for a slightly compressible, unsteady, single-phase reservoir with hydraulic fractures and well models. The equations are then discretized over a triangular, two-dimensional domain using the MFE method, which has been proven to be efficient for flow modelling on irregular grids, as discussed by Vohralík et al. [59], Ewing et al. [88]. The well model selected is based on Darcy's law and incorporated as an additional source term.

From here onward, we will refer to the continuous portion of the reservoir simply as matrix or matrix network. Likewise, the fractured portion of the reservoir will be referred to as fractures or fracture network.

3.1 Governing Equations and Model Description

The governing equations for single-phase flow through porous media is fully defined by Darcy's Law for conservation of momentum, and the Continuity equation for mass conservation. The assumptions used to formulate the model are:

- Negligible gravity effects
- Slightly compressible, single phase flow
- Flow regime is not affected by turbulence effects
- Constant PVT properties
- Two dimensional geometry

With the neglecting of turbulence effects, Darcy's law would not be valid to study shale formations with pore sizes in the nano-metre scale, but would describe tight formations such

as carbonates and impermeable limestones. Turbulent effects could be added to Darcy's law in order to overcome this shortcoming [89].

The equations for the matrix and fracture networks are formulated separately, but they are coupled by a source term that represents the flow between the matrix to the fracture elements.

The governing equations for the matrix and the fracture networks are, respectively:

$$\begin{aligned} \vec{V} &= -\frac{\vec{\vec{K}}}{\mu}\nabla P \\ \phi c_o \frac{\partial P}{\partial t} + \nabla \cdot \vec{V} &= Q_t - Q^{ff} \end{aligned} \tag{3.1}$$

$$\begin{aligned} \vec{V}^f &= -\frac{\vec{\vec{K}}^f}{\mu}\nabla P^f \\ \phi^f c_o^f \frac{\partial P^f}{\partial t} + \nabla \cdot \vec{V}^f &= Q_t^f + Q^{ff} \end{aligned} \tag{3.2}$$

where $\vec{V}$ is the total Darcy Velocity vector, $\vec{\vec{K}}$ is the absolute permeability tensor, μ is the oil viscosity, P is the reservoir pressure, ϕ is the porosity of the reservoir, c_o is the total reservoir compressibility, and Q_t is a general mass source term. The superscript f denotes the fracture network.

In the matrix term, the term Q^{ff} in Equation (3.1) implies that in some instances, flow will travel from the matrix network to the fracture network, so we add this additional source term; which will play a significant role in the coupling of the two networks during the discretization process. This term could be negative under certain conditions, but the form of the term would remain unchanged.

Since fractures are represented as a lower dimensional entity in the physical domain, we account by the flow moving from the matrix cell to the fracture by the additional source term Q^{ff} in Equation (3.2). The present work focuses only on natural and hydraulic fractures as high permeability conduits to aid oil production from ultra-low permeability porous media, and thus instances in which fractures act as flow barriers are not taken into consideration. For a fracture acting as a barrier, we would have to implement the fracture as a wall boundary condition, and while this task is simple at this point I did not include this configuration on the scope of the problem being studied.

Figure 3.1 presents the proposed approach to describe the flow profile from the reservoir matrix to the fracture network. For two adjacent triangular elements, K_+ and K_-, sharing a fracture edge K_f, the flow from matrix to fracture follow the relationship:

$$Q^{ff} = Q_{K_+} + Q_{K_-} \tag{3.3}$$

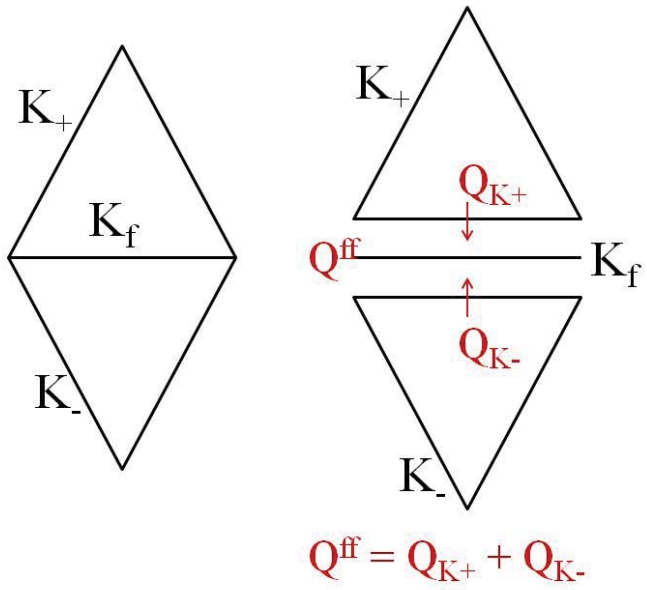

Figure 3.1 – Matrix-fracture discretization interaction, showing the flow going from matrix to fracture and mimicking the flow profile of hydraulic fractures in unconventional reservoirs.

To model the flow from the matrix to the fracture we assume that flow always goes from the matrix to the fracture (the physics of the production process consists on fracture networks interconnected, serving as high conductivity conduit for the oil to move from the ultra low permeability rock into the fracture, and to the production well).

3.2 Discretization using Mixed Finite Element Method

The Mixed Finite Element Method is a technique in which stress fields and displacement fields are both approximated simultaneously as primary variables, as stated by Arnold [90]. In the conventional finite element method, the flux through cell interfaces is obtained after post-processing the pressure field. This method is usually known as the Pressure-Correction Method, extensively described by Connell and Stow [91]. When using mixed finite elements, pressure and fluxes are calculated simultaneously over different solution spaces but using the same computational domain.

To apply the MFE method, the discrete pressure values, a scalar variable) are approximated at the centroid of the triangular elements. The velocity values, which are gradients of the pressure, require a set of vector-based shape functions to complete the MFE formulation. We selected the lowest order Raviart-Thomas elements, RT_0, initially presented by Raviart

and Thomas [46] to study general second order elliptic partial differential equations (PDEs) to discretize the velocity field and complete the MFE formulation. Figure 3.2 presents the RT_0 element and the corresponding lowest-order shape functions, which are outward-pointing vectors coming out perpendicularly from the midpoint of each of the sides of the triangular element. Furthermore, other elements such as Nedelec elements over triangular computational domains can be used to represent similar PDE systems, as initially demonstrated by [92].

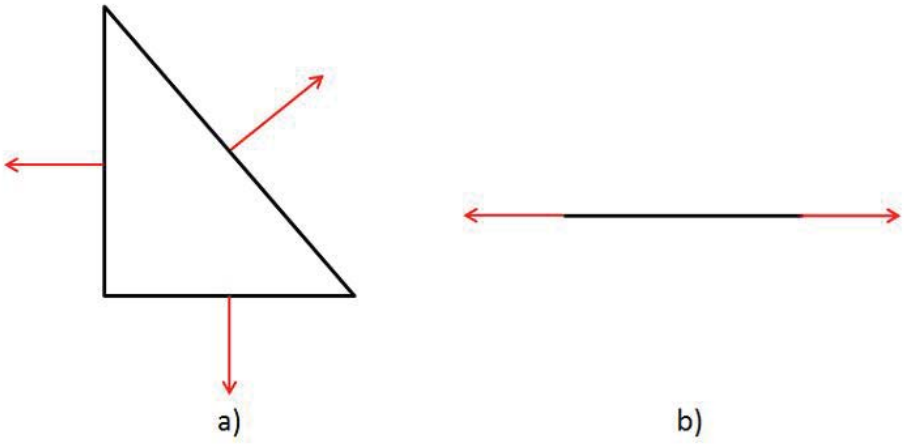

Figure 3.2 – Reference element and degrees of freedom for the lowest order Raviart Thomas MFE triangle in 2D and the simplified implementation for 1D, used for the discretization of the velocity vector field for the matrix and fracture networks.

Consider a general domain with M triangular matrix elements with N edges, and MF number of linear fracture elements with NF edges. Our implementation estimates the average pressure located at the center of the elements, and estimates the velocity at the edges as normal vectors.

To implement the MFE method, the velocity and pressure fields for matrix and fractures, respectively, are discretely represented by:

$$\begin{aligned} \vec{V} &= \sum_{i=1}^{N} v_i \Phi_i \\ P &= \sum_{i=1}^{M} p_i \Psi_i \end{aligned} \tag{3.4}$$

for the matrix grid cells, and

$$\begin{aligned} \vec{V}^f &= \sum_{i=1}^{NF} v_i^f \Phi_i^f \\ P^f &= \sum_{i=1}^{MF} p_i^f \Psi_i^f \end{aligned} \tag{3.5}$$

for the fracture gridcells. The shape functions for the pressure discretization in matrix and fractures are defined as:

$$\Psi_i = \begin{cases} 1 & \text{over triangular element } i \\ 0 & \text{over any other element} \end{cases} \tag{3.6}$$

$$\Psi_i^f = \begin{cases} 1 & \text{over line element } i \\ 0 & \text{over any other element} \end{cases} \tag{3.7}$$

When implementing the MFE method, the interpolation functions for the velocity fields are vector functions. Considering a two dimensional simple domain with two adjacent elements, as shown in Figure 3.3, the RT_0 shape functions for the matrix are then defined as:

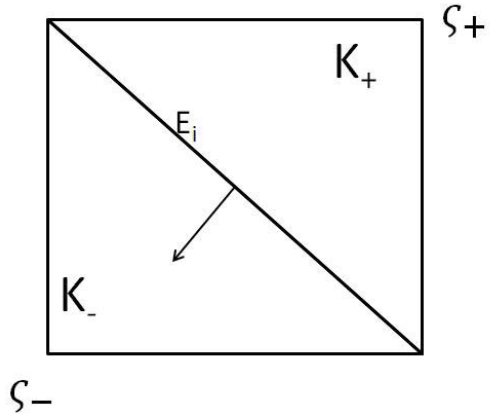

Figure 3.3 – Reference elements K_- and K_+, with shape function defined at edge E_i.

$$\Phi_i = \Phi_i(x) = \begin{cases} \dfrac{|E_i|}{2\,|K_+|}\,(x - \zeta_+) & \text{if } x \in K_+ \\ -\dfrac{|E_i|}{2\,|K_-|}\,(x - \zeta_-) & \text{if } x \in K_- \\ 0 & \text{everywhere else} \end{cases} \tag{3.8}$$

where $|E_i|$ is the length of edge i; $|K_+|$ and $|K_-|$ are the corresponding areas of triangular elements K_+ and K_- respectively; and ζ_+ and ζ_- are the vertex opposite to edge E_i in elements K_+ and K_- respectively. Locally, we can define the RT_0 shape functions as:

$$\Phi_i = \sigma_i \frac{|E_i|}{2\,|K|}\,(x - \zeta) \tag{3.9}$$

in Equation (3.9), σ_i is either 1, -1 or 0 depending on the element location with respect to edge i, as illustrated in Figure 3.3.

The shape functions for the velocity discretization in the fracture network can be similarly formulated for line elements as:

$$\Phi_i^f = \sigma_i^f \frac{1}{2\,|L|}\left(x - \zeta^f\right) \tag{3.10}$$

where σ_i^f is either 1, -1 or 0 depending on the location of x relative to the line edge i, $|L|$ is the length of the line element where the velocity is being interpolated, and ζ^f is the line edge opposite to line edge i.

The variational formulation of the governing equations can be write as:

$$\begin{aligned} &\int \phi\, c_o \frac{\partial P}{\partial t}\Psi_k\, dA + \int \left(\nabla \cdot \vec{V}\right)\Psi_k\, dA = \int Q_T\, \Psi_k\, dA \\ &\int \left(\vec{\vec{m}}^{-1} \cdot \vec{V} + \nabla P\right) \cdot \Phi_k\, dA = 0 \end{aligned} \tag{3.11}$$

$$\begin{aligned} &\int \phi^f\, c_o^f \frac{\partial P^f}{\partial t}\Psi_k^f\, dA + \int \left(\nabla \cdot \vec{V}^f\right)\Psi_k^f\, dA = \int \left(Q_t^f + Q^{ff}\right)\,\Psi_k^f\, dA \\ &\int \left(\vec{\vec{m}}^{f\,-1} \cdot \vec{V}^f + \nabla P^f\right) \cdot \Phi_k^f\, dA = 0 \end{aligned} \tag{3.12}$$

where $\vec{\vec{m}}$ and $\vec{\vec{m}}^f$ are defined as:

$$\vec{\vec{m}} = \frac{\vec{\vec{K}}}{\mu} \qquad \vec{\vec{m}}^f = \frac{\vec{\vec{K}}^f}{\mu} \tag{3.13}$$

and

$$Q_T = Q_t - Q^{ff} \tag{3.14}$$

To handle the effects of representing fractures as lower-dimensional features, for a two-dimensional case we have the following expression to represent the area integral of the fracture:

$$dA = \dashv d\mathcal{L} \tag{3.15}$$

where $\dashv$ represents the fracture aperture and $d\,\mathcal{L}$ represents a line integral. For this thesis, I consider a as a constant value

After some basic rearranging, and omitting the summation signs over all the elements for simplicity, the velocity and pressure approximations can be introduced, and using the Divergence Theorem, Equations (3.11) and (3.12) can be expressed as:

$$\begin{aligned}
&\sum_i v_i \int (\nabla \cdot \Phi_i)\, \Psi_k \, dA + \sum_j \frac{dp_j}{dt} \int \phi \, c_o \Psi_j \, \Psi_k \, dA = \int Q_t \, \Psi_k \, dA \\
&\sum_i v_i \int \left(\vec{\vec{m}}^{-1} \cdot \Phi_j\right) \cdot \Phi_k \, dA - \sum_j p_j \int (\nabla \cdot \Phi_k)\, \Psi_j \, dA = -\int p_b \, (\vec{n} \cdot \Phi_k) \, dl
\end{aligned} \tag{3.16}$$

$$\begin{aligned}
&\sum_i v_i^f \int \left(\nabla \cdot \Phi_i^f\right) \Psi_k^f \, dA + \sum_j \frac{dp_j^f}{dt} \int \phi^f \, c_o^f \Psi_j^f \, \Psi_k^f \, dA = \int \left(Q_t^f + Q^{ff}\right) \, \Psi_k^f \, dA \\
&\sum_i v_i^f \int \left(\vec{\vec{m}} f^{-1} \cdot \Phi_j^f\right) \cdot \Phi_k^f \, dA - \sum_j p_j^f \int \left(\nabla \cdot \Phi_k^f\right) \Psi_j^f \, dA = -\int p_b^f \, \left(\vec{n} \cdot \Phi_k^f\right) \, dl
\end{aligned} \tag{3.17}$$

where p_b and p_b^f represent pressure values prescribed as boundary conditions for the matrix and the fracture networks, respectively. The time derivative of the pressure approximation in Equations(3.16) and (3.17) can be approximated numerically using Taylor series expansion. Due to its simplicity, an implicit backward-differencing scheme where pressure values at the current and previous time-steps is used,

$$\frac{dp}{dt} \approx \frac{p^n - p^{n-1}}{\Delta t} \tag{3.18}$$

where p^n is the pressure value at the current time step, and p^{n-1} represents the pressure value at the previous time step. Next, the governing equations can be approximated by the following linear equations:

$$\begin{aligned}
&\sum_i v_i \int (\nabla \cdot \Phi_i)\, \Psi_k \, dA + \sum_j \frac{p_j^n}{\Delta t} \int \phi \, c_o \Psi_j \, \Psi_k \, dA = \\
&\int Q_t \, \Psi_k \, dA + \sum_j \frac{p_j^{n-1}}{\Delta t} \int \phi \, c_o \Psi_j \, \Psi_k \, dA
\end{aligned} \tag{3.19}$$

$$\sum_i v_i \int \left(\vec{\vec{m}}^{-1} \cdot \Phi_j\right) \cdot \Phi_k \, dA - \sum_j p_j \int (\nabla \cdot \Phi_k)\, \Psi_j \, dA = -\int p_b \, (\vec{n} \cdot \Phi_k) \, dl \tag{3.20}$$

$$\sum_i v_i^f \int \left(\nabla \cdot \Phi_i^f\right) \Psi_k^f \, dA + \sum_j \frac{p_j^{f,n}}{\Delta t} \int \phi^f \, c_o^f \Psi_j^f \, \Psi_k^f \, dA = \int \left(Q_t^f + Q^{ff}\right) \, \Psi_k \, dA + \sum_j \frac{p_j^{f,n-1}}{\Delta t} \int \phi^f \, c_o^f \Psi_j^f \, \Psi_k^f \, dA \tag{3.21}$$

$$\sum_i v_i^f \int \left(\vec{\bar{m}}^{f^{-1}} \cdot \Phi_j^f\right) \cdot \Phi_k^f \, dA - \sum_j p_j^f \int \left(\nabla \cdot \Phi_k^f\right) \Psi_j^f \, dA = - \int p_b^f \, \left(\vec{n} \cdot \Phi_k^f\right) \, dl \tag{3.22}$$

The Q^{ff} term in Equation (3.22) is still defined as previously indicated in Equation (3.3). Finally, the governing equations for matrix and fracture networks, for a single element, can be assembled into the following linear system of equations:

$$\begin{bmatrix} A & B & 0 & 0 \\ C & D & 0 & 0 \\ E^f & 0 & A^f & B^f \\ 0 & 0 & C^f & D^f \end{bmatrix} \begin{pmatrix} v \\ p \\ v^f \\ p^f \end{pmatrix} = \begin{pmatrix} r_1 \\ r_2 \\ r_1^f \\ r_2^f \end{pmatrix} \tag{3.23}$$

where after omitting the summation signs the non-zero entries of the sub-matrices are:

$$A = \sum_i \int \left(\nabla \cdot \Phi_i\right) \Psi_k \, dA \tag{3.24}$$

$$B = \sum_j \frac{1}{\Delta t} \int \phi \, c_o \Psi_j \, \Psi_k \, dA \tag{3.25}$$

$$C = \sum_i \int \left(\vec{\bar{m}}^{-1} \cdot \Phi_j\right) \cdot \Phi_k \, dA \tag{3.26}$$

$$D = -\sum_j \int \left(\nabla \cdot \Phi_k\right) \Psi_j \, dA \tag{3.27}$$

$$A^f = \sum_i \int \left(\nabla \cdot \Phi_i^f\right) \Psi_k^f \, dA \tag{3.28}$$

$$B^f = \sum_j \frac{1}{\Delta t} \int \phi^f \, c_o^f \Psi_j^f \, \Psi_k^f \, dA \tag{3.29}$$

$$C^f = \sum_i \int \left(\vec{\bar{m}}^{f^{-1}} \cdot \Phi_j^f\right) \cdot \Phi_k^f \, dA \tag{3.30}$$

$$D^f = -\sum_j \int \left(\nabla \cdot \Phi_k^f\right) \Psi_j^f \, dA \tag{3.31}$$

$$r_1 = \int Q_t \, \Psi_k \, dA + \sum_j \frac{p_j^{n-1}}{\Delta t} \int \phi \, c_o \Psi_j \, \Psi_k \, dA \tag{3.32}$$

$$r_2 = - \int p_b \, (\vec{n} \cdot \Phi_k) \, dl \tag{3.33}$$

$$r_1^f = \int \left(Q_t^f + Q^{ff} \right) \, \Psi_k \, dA + \sum_j \frac{p_j^{f,n-1}}{\Delta t} \int \phi^f \, c_o^f \Psi_j^f \, \Psi_k^f \, dA \tag{3.34}$$

$$r_2^f = - \int p_b^f \, \left(\vec{n} \cdot \Phi_k^f \right) \, dl \tag{3.35}$$

and the non-zero entries of matrix E^f are given by:

$$E_{i,j}^f = \begin{bmatrix} |E_i| & |E_j| \end{bmatrix} \tag{3.36}$$

Thus, the resulting linear system for all elements in the computational domain is of size $M + N + MF + NF$. The selected Raviart-Thomas shape functions have the following properties, which are useful to compute exact solutions for the integrals in Equations (3.24) to (3.36):

$$\nabla \cdot \Phi_i = \begin{cases} \sigma_i \dfrac{|E_i|}{|K|} & \text{on element } K \\ 0 & \text{elsewhere} \end{cases} \tag{3.37}$$

$$\nabla \cdot \Phi_j^f = \begin{cases} \sigma_j^f \dfrac{2}{|E_j|} & \text{on line element } j \\ 0 & \text{elsewhere} \end{cases} \tag{3.38}$$

$$\vec{n} \cdot \Phi_i = \begin{cases} 1 & \text{along edge } i \\ 0 & \text{along any other edge} \end{cases} \tag{3.39}$$

$$\vec{n} \cdot \Phi_j^f = \begin{cases} \dfrac{1}{2} & \text{on line vertex } j \\ 0 & \text{on any other line vertex} \end{cases} \tag{3.40}$$

The computational domains for all cases were created using GMSH, a grid generator tailored specifically for Finite Element applications [78]. We selected the Delaunay triangulation meshing scheme [93, 94] to create the discrete triangular elements.

Using the expressions and identities from Equations (3.37) to (3.40), the integrals presented in Equations (3.24) to (3.35) have an exact analytical form. For a typical system, most coefficient entries of the sub-matrices represented by Equations (3.24) to (3.35) will be zero. The non-zero entries for the global system of equations are given by:

$$\hat{A} = \int (\nabla \cdot \Phi_i)\, \Psi_k \, dA = \sigma_i |E_i| \tag{3.41}$$

which has a size of $M \times N$ and which non-zero entries will happen only when triangular element i contains edge k,

$$\hat{B} = \frac{1}{\Delta t} \int \phi \, c_o \Psi_j \, \Psi_k \, dA = \frac{\phi \, c_o}{\Delta t} |K| \tag{3.42}$$

which has a size of $M \times M$ and is a diagonal matrix. The diagonal terms survive just because of the fact that the term $\Psi_j \, \Psi_k$ is equivalent to $\delta_{j,k}$,

$$\begin{aligned} \hat{C} &= \int \left(\vec{\vec{m}}^{-1} \cdot \Phi_j \right) \cdot \Phi_k \, dA \\ &= \frac{\mu_o}{k_m} \sum_{j=1}^{3} \sum_{k=1}^{3} \sigma_j \, \sigma_k \frac{|E_j||E_k|}{4 \, |K_{j,k \, \in \, K}|^2} \int (x - \zeta_j) \cdot (x - \zeta_k) \, dA \end{aligned} \tag{3.43}$$

is a squared matrix of size $N \times N$ and has an integral of a quadratic function over a triangular element; which can be readily solved using quadrature rules and the term k_m is the matrix permeability (assumed to be constant),

$$\hat{D} = - \int (\nabla \cdot \Phi_k)\, \Psi_j \, dA = -\hat{A}^T \tag{3.44}$$

is a matrix of size $N \times M$, and is the negative transpose of matrix $\hat{A}$. The vector $\hat{r_1}$ is of length M, and is defined as:

$$\begin{aligned} \hat{r_1} &= \left[\int \left(Q_t - Q^{ff} \right) \, \Psi_k \, dA + \frac{p_j^{n-1}}{\Delta t} \int \phi \, c_o \Psi_j \, \Psi_k \, dA \right] \\ &= \left(Q_t + \phi \, c_o \frac{p_j^{n-1}}{\Delta t} \right) |K| - \int Q^{ff} \Psi_k \, dA \end{aligned} \tag{3.45}$$

where the term Q^{ff} will require special attention, similar to the implementation of certain boundary conditions. These conditions are explained in Section 3.4. Similarly, the vector $\hat{r_2}$ is of length N, and is defined as:

$$\hat{r_2} = - \int p_b \, (\vec{n} \cdot \Phi_k) \, dl = -p_b |E_k| \tag{3.46}$$

The matrix $\hat{A^f}$, of size $MF \times NF$, is the counterpart of matrix $\hat{A}$ for the fracture network. It takes the following form:

$$\hat{A^f} = \int \left(\nabla \cdot \Phi_i^f \right) \Psi_k^f \, dA = 2 \, \sigma_i^f \tag{3.47}$$

Matrix $\hat{B^f}$ is a diagonal matrix of size $MF \times MF$, and the non-zero elements are given by:

$$\hat{B^f} = \frac{1}{\Delta t} \int \phi^f \, c_o^f \Psi_j^f \, \Psi_k^f \, dA = \frac{\phi^f \, c_o^f}{\Delta t} |E| \tag{3.48}$$

Matrix $\hat{C^f}$ has a size of $NF \times NF$, and the corresponding non-zero entries are given by:

$$\begin{aligned} \hat{C^f} &= \int \left(\vec{\vec{m}}^{f^{-1}} \cdot \Phi_j^f \right) \cdot \Phi_k^f \, dA \\ &= \sigma j^f \sigma_k^f \sum_{j=1}^{2} \sum_{k=1}^{2} \frac{\mu_o}{4 \, k_f \, |E_j| \, |E_k|} \int \left(x - \zeta_j^f \right) \cdot \left(x - \zeta_k^f \right) dA \end{aligned} \tag{3.49}$$

where k_f is the absolute permeability of the fracture network which is assumed to be constant across the computational domain. The area integral of the fracture elements are defined as lines, thus exact solutions for the integral of this quadratic function can be obtained using quadrature rules.
Matrix $\hat{D^f}$ has a size of $NF \times MF$, and the non-zero terms are given by:

$$\hat{D^f} = - \int \left(\nabla \cdot \Phi_k^f \right) \Psi_j^f \, dA = -\hat{A^f}^T \tag{3.50}$$

The non-zero entries corresponding to the vectors $\hat{r_1^f}$ and $\hat{r_2^f}$ are given by:

$$\begin{aligned} \hat{r_1^f} &= \int \left(Q_t^f + Q^{ff} \right) \Psi_k \, dA + \frac{p_j^{f,n-1}}{\Delta t} \int \phi^f \, c_o^f \Psi_j^f \, \Psi_k^f \, dA \\ &= \left(Q_t^f + \phi^f \, c_o^f \frac{p_j^{f,n-1}}{\Delta t} \right) |E| + \int Q^{ff} \Psi_k^f \, dA \end{aligned} \tag{3.51}$$

$$\hat{r_2^f} = - \int p_b^f \left(\vec{n} \cdot \Phi_k^f \right) dl = -\frac{p_b^f}{2} \tag{3.52}$$

where vector $\hat{r_1^f}$ is of size MF and vector $\hat{r_2^f}$ is of size NF. If no pressure boundary condition is prescribed on the fracture network, the value of $\hat{r_2^f}$ is equal to zero.

Thus, the preliminary of the solution matrix for this thesis is given by a linear system of the following form, once we ignore boundary conditions, well models and matrix-fracture interactions:

$$\begin{bmatrix} \hat{A} & \hat{B} & 0 & 0 \\ \hat{C} & \hat{D} & 0 & 0 \\ 0 & 0 & \hat{A^f} & \hat{B^f} \\ 0 & 0 & \hat{C^f} & \hat{D^f} \end{bmatrix} \begin{pmatrix} v \\ p \\ v^f \\ p^f \end{pmatrix} = \begin{pmatrix} \hat{r_1} \\ \hat{r_2} \\ \hat{r_1^f} \\ \hat{r_2^f} \end{pmatrix} \tag{3.53}$$

The special considerations that must be taken into account to solve the complete system of equations while implementing boundary conditions, as well as the final form of the term Q^{ff} are further explained in Section 3.4.

With this formulation I do not require grid refinement in order to represent fractures of any aperture size. Therefore, the computational efficiency from the space allocation and memory management of the developed numerical framework is superior to the schemes present in a software such as COMSOL. If no fractures are present and a grid with the same order of elements is used, the MFE model will be at a disadvantage when compared to COMSOL, because while the number of unknowns of COMSOL will be $2E$ (where E represents the number of edges/vertex of the computational domain), the MFE formulation will require $K + 3E$ unknowns (where K is the number of triangular elements in the computational domain).

3.3 Point-Source Well Model

Well models are incorporated using a point-source approach based on Darcy's Law. Wells are to be located at a hydraulic fracture, so cases where the well is located in the matrix network are not taken into consideration in our proposed formulation. Similar to the assumption used by Bai et al. [67], flow to the well is only fed by the fractures and not the matrix. Consider the diagram shown in Figure 3.4, where two adjacent fractures share a point-source, pressure constrained production well. The flow coming from both fracture elements to the well is approximated using superposition by:

$$Q_w = -\frac{k_1}{A_1\,\mu\,\Delta L_1}\,(p_1 - p_{wf}) - \frac{k_2}{A_2\,\mu\,\Delta L_2}\,(p_2 - p_{wf}) \tag{3.54}$$

where A is the flow cross sectional area and ΔL is the fracture half length. Assuming equal fracture permeabilities, uniform aperture size and same half length (which is controlled by the meshing algorithm), we have the following:

$$Q_w = \frac{k}{A\,\mu\,\Delta L}\,(p_1 + p_2 - 2p_{wf}) = 2\frac{k}{A\,\mu\,\Delta L}\left(\frac{p_1 + p_2}{2} - p_{wf}\right) \tag{3.55}$$

$$Q_w = \frac{2\,k}{A\,\mu\,\Delta L}\,(\bar{p} - p_{wf}) = J\,(\bar{p} - p_{wf}) \tag{3.56}$$

Since J is constant, we have a formulation that relates the flow to the pressure values of the fractures connected to the well. The same procedure can be utilized to place a well model at an intersection of three or more fractures, for nf fractures the general form of the well model will be:

$$Q_w = \frac{nf\,k}{A\,\mu\,\Delta L}\left(\frac{\sum_{i=1}^{nf} p_i}{nf} - p_{wf}\right) \tag{3.57}$$

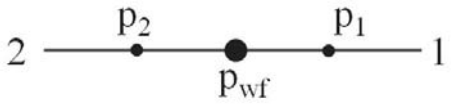

Figure 3.4 – Connected hydraulic fractures with pressure driven well.

To validate the analytical expression we used to define our well model, we set up a CMG IMEX simulation and plotted oil rate at Reservoir Conditions (units of m^3/s)versus Δp, where

$$\Delta p = p - p_{wf} \tag{3.58}$$

We used a linear fit on the obtained profile, and estimated the value of J as the slope of the linearisation of oil rate versus Δp. Figure 3.5 presents the procedure described on this section, where we can identify the predicted value of J to be $2.72 \times 10^{-11}\,m^3\,Pa^{-1}\,s^{-1}$. Additionally, we can see that the estimated intersect in the y-axis of the generated plot is $6.56 \times 10^{-14} m^3/s$, which means the form of the predicted curve is very similar to that described by Equation (3.57) and the intersect is negligible. Finally, we can see the R^2 value of the linear fit is 1.00, meaning that our linear equation is able to describe the data to a nearly perfect fit for early production times.

From the well model, we compared the expression we use to compute J from Equation (3.57) as a function of grid size, along with the single point obtained from CMG IMEX. Figure 3.6 demonstrates that our proposed well model is in very good agreement with the J value obtained after linearisation of the flow rate versus pressure difference. Our algebraic model under predicted the value J to be $2.50 \times 10^{-11}\,m^3\,Pa^{-1}\,s^{-1}$, which is within 8% of the value that resulted from the CMG IMEX simulation setup. While this difference will certainly cause our numerical results to slightly underpredict oil production rates, the estimates from our mixed finite element formulation coupled with this algebraic point-source well model will fit well in between a satisfactory margin or error.

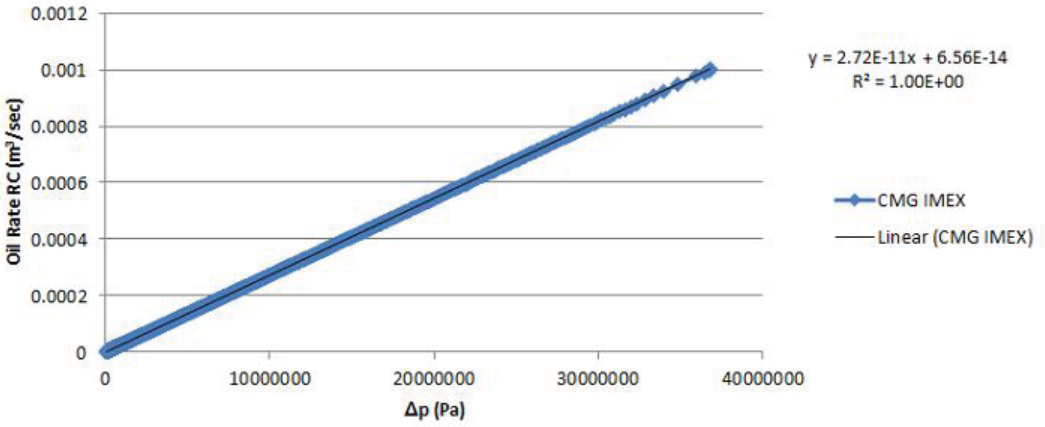

Figure 3.5 – Scatter plot of oil rate versus Δp from CMG IMEX, linear fit, and R^2 value for early production times.

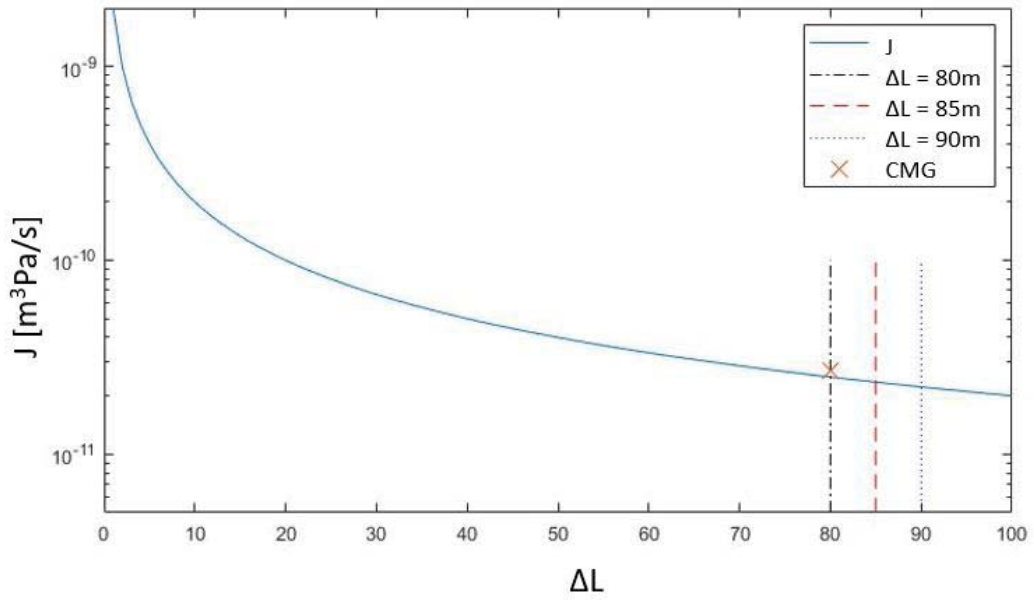

Figure 3.6 – J as a function of fracture half length, compared with CMG IMEX production profile.

3.4 Special Considerations of Modelling Approach

To complete the formulation presented in Equation (3.53), we must consider three separate scenarios:

- Boundary conditions
- Well models
- Q^{ff}, the matrix-fracture interactions

3.4.1 Special Case: Boundary Conditions

Pressure conditions prescribed at the boundaries of the proposed model are called natural boundary conditions, because they become part of the model formulation itself. We have a tern p_b, which is only non-zero at the boundaries where the pressure is prescribed. To implement prescribed values for fluxes and velocities at the boundaries, the linear system of equations needs to be modified. The no slip condition at the walls is a clear example of this special case of boundary conditions. The basic form of these equations is:

$$v_{boundary} = v_o \tag{3.59}$$

where v_o is the velocity value prescribed at the boundary. Figure 3.7 shows a simple, unfractured reservoir and how the linear system of equations will look like under normal pressure-driven conditions, and Figure 3.8 shows how a wall boundary condition is implemented; the terms affected by these are sub-matrices $\hat{C}$ and $\hat{D}$, and the vector $\hat{r_2}$.

3.4.2 Special Case: Well Models

Consider the diagram presented in Figure 3.4, where two intersecting fractures share a pressure-controlled well. For a case of only two fractures, Equation (3.56) can be written as:

$$Q_w = J\left(\frac{p_1^f + p_2^f}{2} - p_{wf}\right) \tag{3.60}$$

$$Q_w = \frac{v_w}{AC_f} = J\,\frac{p_1^f}{2} + J\,\frac{p_2^f}{2} - J\,p_{wf} \tag{3.61}$$

where AC_f is the flow cross sectional area of the fractures. This leads to an expression that relates the velocity (our solution variable) to the adjacent fracture pressures:

$$v_w = J\,AC_f\,\frac{p_1^f}{2} + J\,AC_f\,\frac{p_2^f}{2} - J\,AC_f\,p_{wf} \tag{3.62}$$

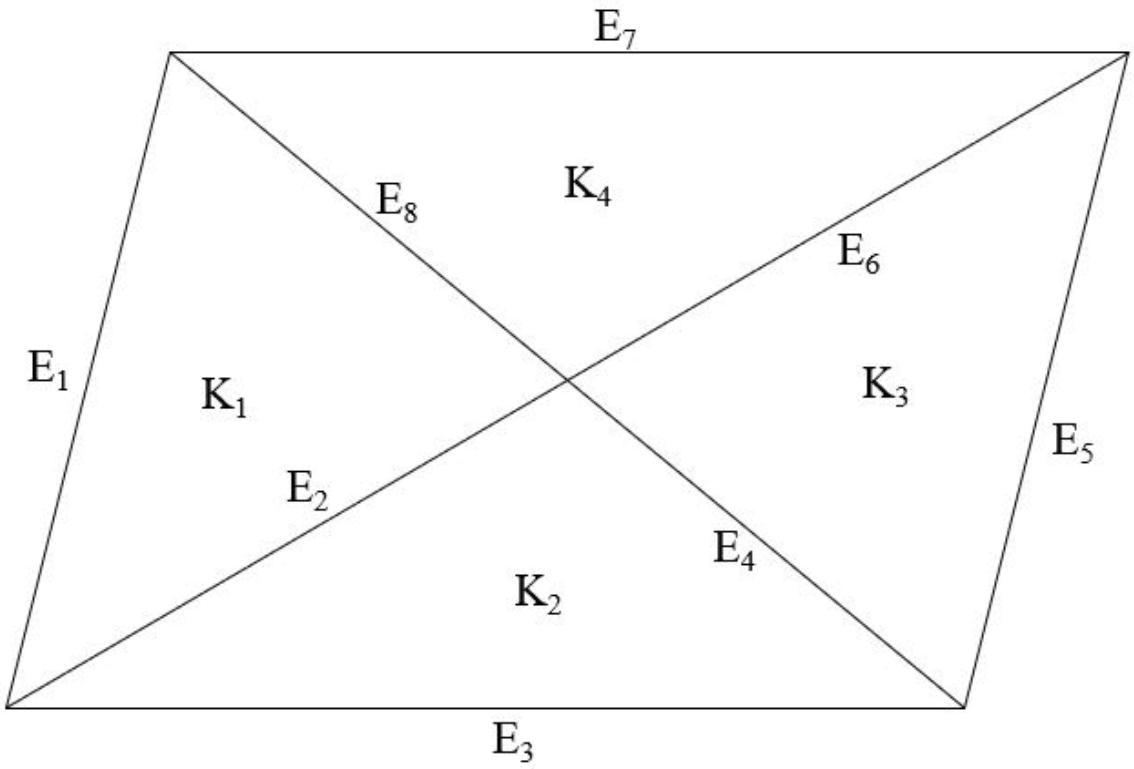

$$\begin{bmatrix} \hat{A_{11}} & \hat{A_{12}} & \hat{A_{13}} & \hat{A_{14}} & \hat{A_{15}} & \hat{A_{16}} & \hat{A_{17}} & \hat{A_{18}} & \hat{B_{11}} & \hat{B_{12}} & \hat{B_{13}} & \hat{B_{14}} \\ \hat{A_{21}} & \hat{A_{22}} & \hat{A_{23}} & \hat{A_{24}} & \hat{A_{25}} & \hat{A_{26}} & \hat{A_{27}} & \hat{A_{28}} & \hat{B_{21}} & \hat{B_{22}} & \hat{B_{23}} & \hat{B_{24}} \\ \hat{A_{31}} & \hat{A_{32}} & \hat{A_{33}} & \hat{A_{34}} & \hat{A_{35}} & \hat{A_{36}} & \hat{A_{37}} & \hat{A_{38}} & \hat{B_{31}} & \hat{B_{32}} & \hat{B_{33}} & \hat{B_{34}} \\ \hat{A_{41}} & \hat{A_{42}} & \hat{A_{43}} & \hat{A_{44}} & \hat{A_{45}} & \hat{A_{46}} & \hat{A_{47}} & \hat{A_{48}} & \hat{B_{41}} & \hat{B_{42}} & \hat{B_{43}} & \hat{B_{44}} \\ \hat{C_{11}} & \hat{C_{12}} & \hat{C_{13}} & \hat{C_{14}} & \hat{C_{15}} & \hat{C_{16}} & \hat{C_{17}} & \hat{C_{18}} & \hat{D_{11}} & \hat{D_{12}} & \hat{D_{13}} & \hat{D_{14}} \\ \hat{C_{21}} & \hat{C_{22}} & \hat{C_{23}} & \hat{C_{24}} & \hat{C_{25}} & \hat{C_{26}} & \hat{C_{27}} & \hat{C_{28}} & \hat{D_{21}} & \hat{D_{22}} & \hat{D_{23}} & \hat{D_{24}} \\ \hat{C_{31}} & \hat{C_{32}} & \hat{C_{33}} & \hat{C_{34}} & \hat{C_{35}} & \hat{C_{36}} & \hat{C_{37}} & \hat{C_{38}} & \hat{D_{31}} & \hat{D_{32}} & \hat{D_{33}} & \hat{D_{34}} \\ \hat{C_{41}} & \hat{C_{42}} & \hat{C_{43}} & \hat{C_{44}} & \hat{C_{45}} & \hat{C_{46}} & \hat{C_{47}} & \hat{C_{48}} & \hat{D_{41}} & \hat{D_{42}} & \hat{D_{43}} & \hat{D_{44}} \\ \hat{C_{51}} & \hat{C_{52}} & \hat{C_{53}} & \hat{C_{54}} & \hat{C_{55}} & \hat{C_{56}} & \hat{C_{57}} & \hat{C_{58}} & \hat{D_{51}} & \hat{D_{52}} & \hat{D_{53}} & \hat{D_{54}} \\ \hat{C_{61}} & \hat{C_{62}} & \hat{C_{63}} & \hat{C_{64}} & \hat{C_{65}} & \hat{C_{66}} & \hat{C_{67}} & \hat{C_{68}} & \hat{D_{61}} & \hat{D_{62}} & \hat{D_{63}} & \hat{D_{64}} \\ \hat{C_{71}} & \hat{C_{72}} & \hat{C_{73}} & \hat{C_{74}} & \hat{C_{75}} & \hat{C_{76}} & \hat{C_{77}} & \hat{C_{78}} & \hat{D_{71}} & \hat{D_{72}} & \hat{D_{73}} & \hat{D_{74}} \\ \hat{C_{81}} & \hat{C_{82}} & \hat{C_{83}} & \hat{C_{84}} & \hat{C_{85}} & \hat{C_{86}} & \hat{C_{87}} & \hat{C_{88}} & \hat{D_{81}} & \hat{D_{82}} & \hat{D_{83}} & \hat{D_{84}} \end{bmatrix} \begin{pmatrix} v_1 \\ v_2 \\ v_3 \\ v_4 \\ v_5 \\ v_6 \\ v_7 \\ v_8 \\ p_1 \\ p_2 \\ p_3 \\ p_4 \end{pmatrix} = \begin{pmatrix} r_{1,1} \\ r_{1,2} \\ r_{1,3} \\ r_{1,4} \\ r_{2,1} \\ r_{2,2} \\ r_{2,3} \\ r_{2,4} \\ r_{2,5} \\ r_{2,6} \\ r_{2,7} \\ r_{2,8} \end{pmatrix}$$

Figure 3.7 – Simple mesh with 4 triangular elements and 8 edges, and no fractures; and the shape of the corresponding system of linear equations with no boundary conditions prescribed.

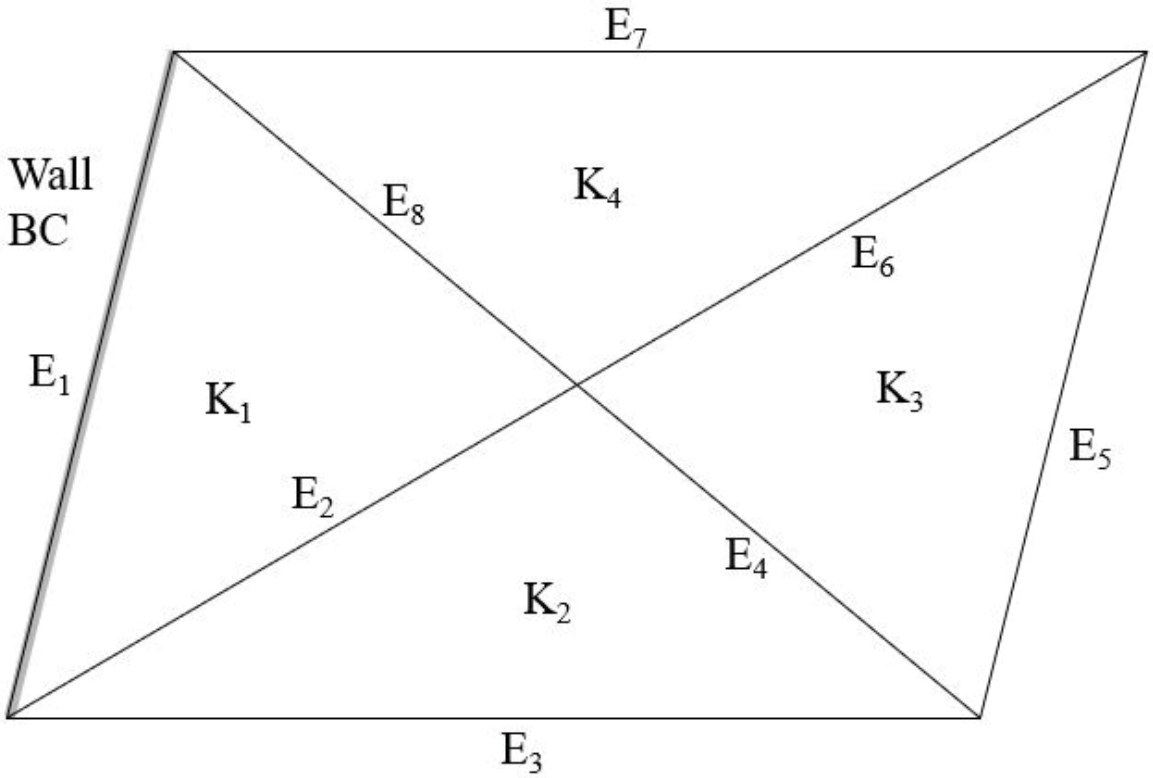

$$\begin{bmatrix}
\hat{A}_{11} & \hat{A}_{12} & \hat{A}_{13} & \hat{A}_{14} & \hat{A}_{15} & \hat{A}_{16} & \hat{A}_{17} & \hat{A}_{18} & \hat{B}_{11} & \hat{B}_{12} & \hat{B}_{13} & \hat{B}_{14} \\
\hat{A}_{21} & \hat{A}_{22} & \hat{A}_{23} & \hat{A}_{24} & \hat{A}_{25} & \hat{A}_{26} & \hat{A}_{27} & \hat{A}_{28} & \hat{B}_{21} & \hat{B}_{22} & \hat{B}_{23} & \hat{B}_{24} \\
\hat{A}_{31} & \hat{A}_{32} & \hat{A}_{33} & \hat{A}_{34} & \hat{A}_{35} & \hat{A}_{36} & \hat{A}_{37} & \hat{A}_{38} & \hat{B}_{31} & \hat{B}_{32} & \hat{B}_{33} & \hat{B}_{34} \\
\hat{A}_{41} & \hat{A}_{42} & \hat{A}_{43} & \hat{A}_{44} & \hat{A}_{45} & \hat{A}_{46} & \hat{A}_{47} & \hat{A}_{48} & \hat{B}_{41} & \hat{B}_{42} & \hat{B}_{43} & \hat{B}_{44} \\
1 & 0 & 0 & 0 & 0 & 0 & 0 & 0 & 0 & 0 & 0 & 0 \\
\hat{C}_{21} & \hat{C}_{22} & \hat{C}_{23} & \hat{C}_{24} & \hat{C}_{25} & \hat{C}_{26} & \hat{C}_{27} & \hat{C}_{28} & \hat{D}_{21} & \hat{D}_{22} & \hat{D}_{23} & \hat{D}_{24} \\
\hat{C}_{31} & \hat{C}_{32} & \hat{C}_{33} & \hat{C}_{34} & \hat{C}_{35} & \hat{C}_{36} & \hat{C}_{37} & \hat{C}_{38} & \hat{D}_{31} & \hat{D}_{32} & \hat{D}_{33} & \hat{D}_{34} \\
\hat{C}_{41} & \hat{C}_{42} & \hat{C}_{43} & \hat{C}_{44} & \hat{C}_{45} & \hat{C}_{46} & \hat{C}_{47} & \hat{C}_{48} & \hat{D}_{41} & \hat{D}_{42} & \hat{D}_{43} & \hat{D}_{44} \\
\hat{C}_{51} & \hat{C}_{52} & \hat{C}_{53} & \hat{C}_{54} & \hat{C}_{55} & \hat{C}_{56} & \hat{C}_{57} & \hat{C}_{58} & \hat{D}_{51} & \hat{D}_{52} & \hat{D}_{53} & \hat{D}_{54} \\
\hat{C}_{61} & \hat{C}_{62} & \hat{C}_{63} & \hat{C}_{64} & \hat{C}_{65} & \hat{C}_{66} & \hat{C}_{67} & \hat{C}_{68} & \hat{D}_{61} & \hat{D}_{62} & \hat{D}_{63} & \hat{D}_{64} \\
\hat{C}_{71} & \hat{C}_{72} & \hat{C}_{73} & \hat{C}_{74} & \hat{C}_{75} & \hat{C}_{76} & \hat{C}_{77} & \hat{C}_{78} & \hat{D}_{71} & \hat{D}_{72} & \hat{D}_{73} & \hat{D}_{74} \\
\hat{C}_{81} & \hat{C}_{82} & \hat{C}_{83} & \hat{C}_{84} & \hat{C}_{85} & \hat{C}_{86} & \hat{C}_{87} & \hat{C}_{88} & \hat{D}_{81} & \hat{D}_{82} & \hat{D}_{83} & \hat{D}_{84}
\end{bmatrix}
\begin{pmatrix} v_1 \\ v_2 \\ v_3 \\ v_4 \\ v_5 \\ v_6 \\ v_7 \\ v_8 \\ p_1 \\ p_2 \\ p_3 \\ p_4 \end{pmatrix}
=
\begin{pmatrix} r_{1,2} \\ r_{1,2} \\ r_{1,3} \\ r_{1,4} \\ 0 \\ r_{2,2} \\ r_{2,3} \\ r_{2,4} \\ r_{2,5} \\ r_{2,6} \\ r_{2,7} \\ r_{2,8} \end{pmatrix}$$

Figure 3.8 – Simple mesh with 4 triangular elements and 8 edges, and no fractures; and the shape of the corresponding system of linear equations with wall boundary conditions prescribed at Edge # 1.

Each pressure controlled well will have a corresponding equation of the same form. This equation will replace a complete row in Equation (3.53), involving the sub-matrices $\hat{C}^f$ and $\hat{D}^f$, and the vector $\hat{r_2^f}$. An example of this special condition is illustrated in Figure 3.9, and the linear system of equations for this condition are shown in Figure 3.10, where for convenience we neglected the Q^{ff} terms who capture the matrix-fracture interactions.

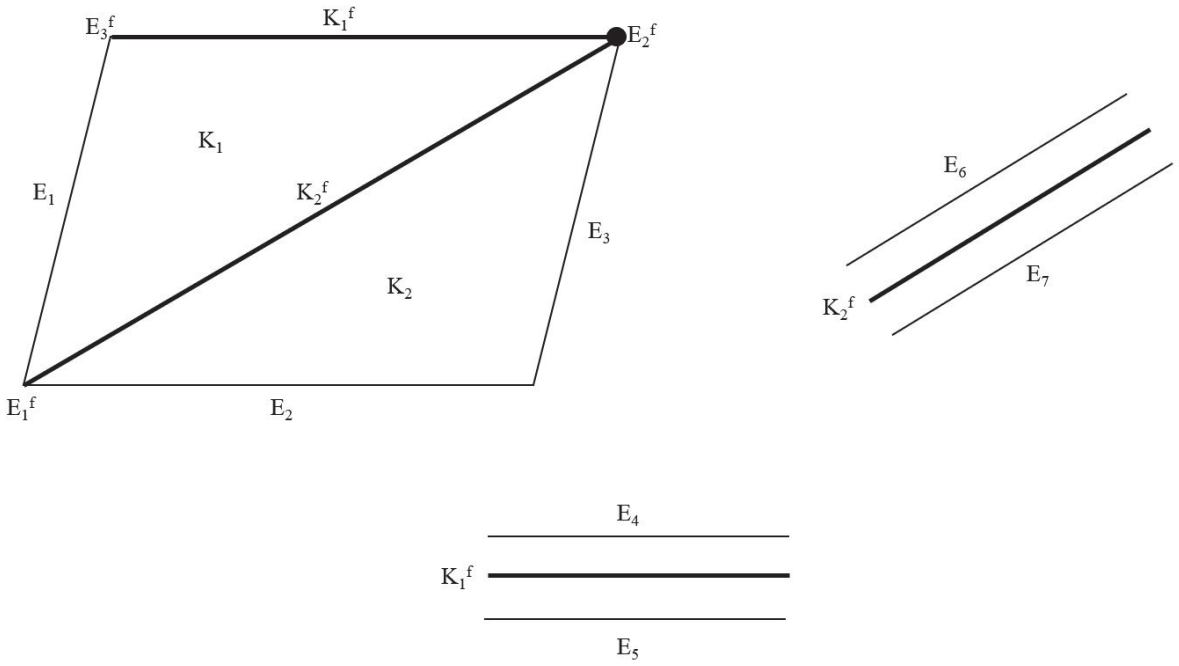

Figure 3.9 – Simple mesh with 2 triangular elements, 7 matrix edges, 2 fracture elements, 3 fracture edges, and a single well.

3.4.3 Special Case: Matrix-Fracture Interaction

The matrix-fracture interactions are captured by the term Q^{ff}, and this term is present in both the matrix mass conservation and the fracture mass conservation. As indicated in Equation (3.3), the term Q^{ff} is expressed as a function of fluxes. To use the solution variables, which are pressures and velocities, we can rewrite Equation (3.3) as:

$$Q^{ff} = v_{K+}\, AC_{mf} + v_{K-}\, AC_{mf} \tag{3.63}$$

where AC_{mf} is the cross sectional area between the matrix and the fractures. In two-dimensional domains, this cross sectional area is equal to the fracture length multiplied by the reservoir thickness. For this studies, we assume a unit thickness for all calculations. Since the length of the fracture element is the same as the length of the edge elements where the fracture is defined, the previous equation can be re-written as:

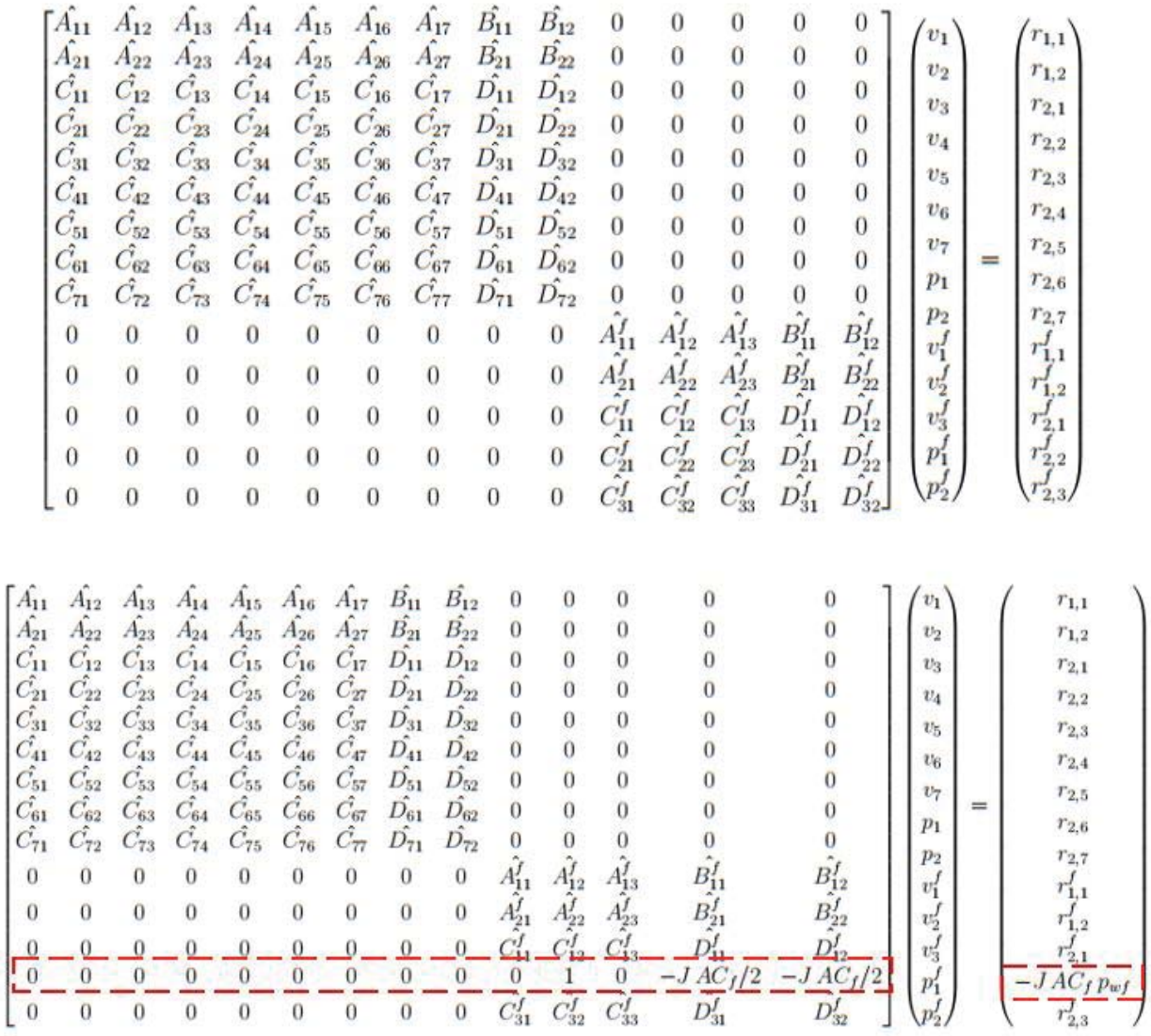

Figure 3.10 – Linear system of equations demonstrating how well boundary conditions are incorporated with the DFN model. Top: default systems of equations. Bottom: systems of equations with the well model.

$$Q^{ff} = v_{K+} |E_{f,+}| + v_{K-} |E_{f,-}| \tag{3.64}$$

where $|E_{f,+}|$ and $|E_{f,-}|$ are the edges where the velocities v_{K+} and v_{K-} are defined, respectively. While treated as different edges, $|E_{f,+}|$ and $|E_{f,-}|$ have the same length. When we incorporate these terms on the matrix network, sub-matrix $\hat{A}$, and vector $\hat{r_1}$ are affected. While the form of sub-matrix $\hat{A}$ remains almost identical to previous cases where fractures are not present, the velocity at edges E_8 and E_9 is assumed to be always going from the matrix to the fracture; and we do this by always assigning a positive sign to the corresponding shape functions for the edge velocities v_8 and v_9.

When we incorporate the effects described by Equation (3.3), the vector $\hat{r_1^f}$ will be modified, and additional terms we combine into sub-matrix $\hat{E^f}$ will be introduced into the linear system in Equation (3.53):

$$\begin{bmatrix} \hat{A} & \hat{B} & 0 & 0 \\ \hat{C} & \hat{D} & 0 & 0 \\ \hat{E^f} & 0 & \hat{A^f} & \hat{B^f} \\ 0 & 0 & \hat{C^f} & \hat{D^f} \end{bmatrix} \begin{pmatrix} v \\ p \\ v^f \\ p^f \end{pmatrix} = \begin{pmatrix} \hat{r_1} \\ \hat{r_2} \\ \hat{r_1^f} \\ \hat{r_2^f} \end{pmatrix} \tag{3.65}$$

An example of a simple mesh with 4 matrix elements, 1 fracture element, 9 matrix edges and 2 fracture edges is shown in Figure 3.11. The shape of the linear systems of equations and the sub-matrix $\hat{E^f}$ is shown in Figure 3.12, where for convenience the effects of flux/velocity boundary conditions and well models are neglected.

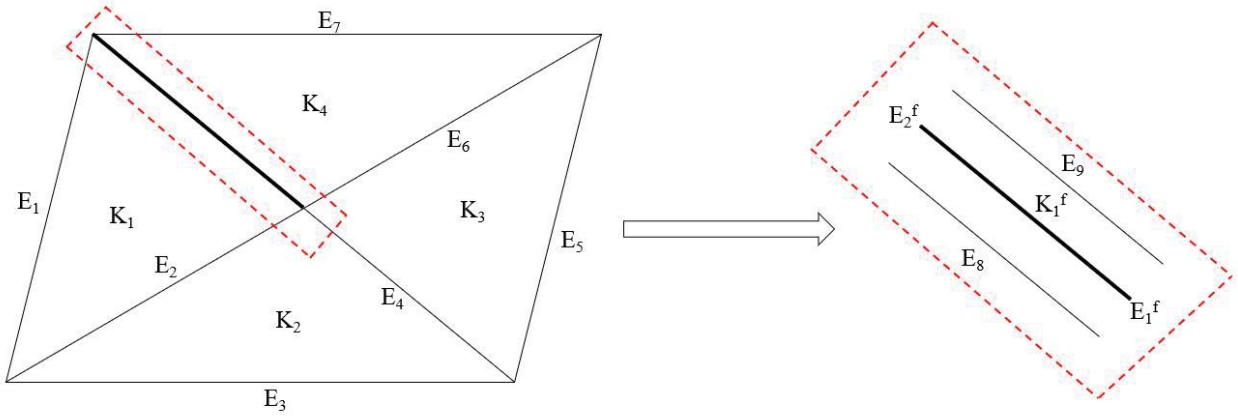

Figure 3.11 – Sample mesh with four triangular matrix elements and a single fracture element to illustrate the matrix-fracture interactions.

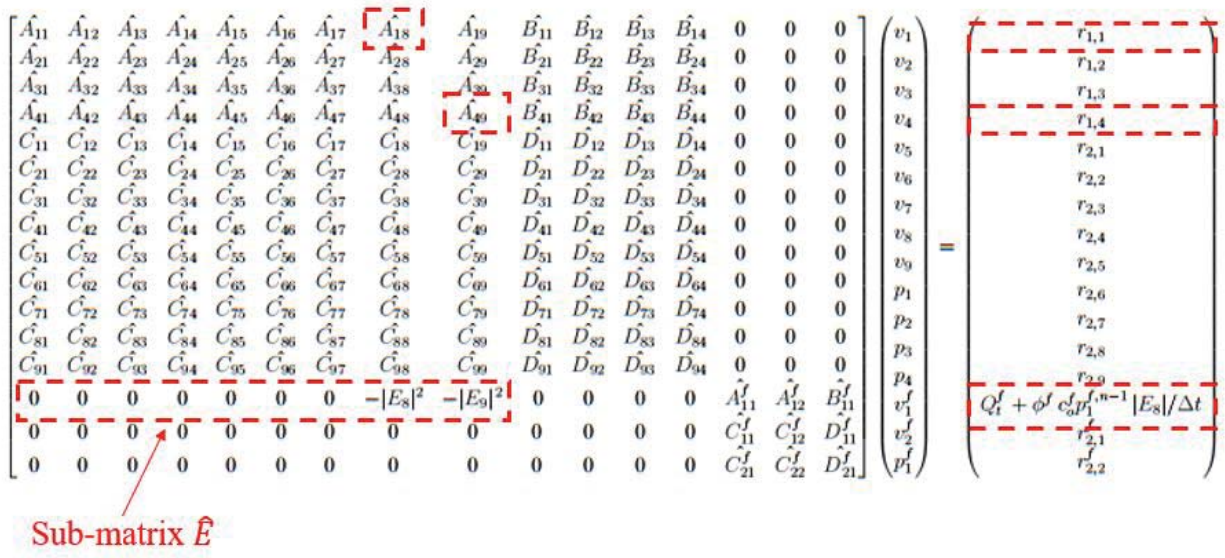

Figure 3.12 – General form of the linear system of equations for a fractured reservoir, ignoring effects of flux/velocity boundary conditions and well models.

3.5 Framework Diagram and Project Strategy

The schematic diagram showing the flow of the framework we developed to study tight reservoirs with multiscale fractures is presented in Figure 3.13. Although other alternatives exist, we selected FORTRAN [95–97] as the programming language for the computational framework, GMSH [78] as the unstructured mesh generation, and VisIT [98] as the scientific visualization tool.

Figure 3.14 presents the schematic diagram for the completion of the proposed thesis. Once the proposed discrete fracture network model is developed, we implement a multi-step validation process with commercial simulation packages. Once the solvers developed in-house are validated, we then present the comparisons between fracture configurations and the impact of fracture orientation.

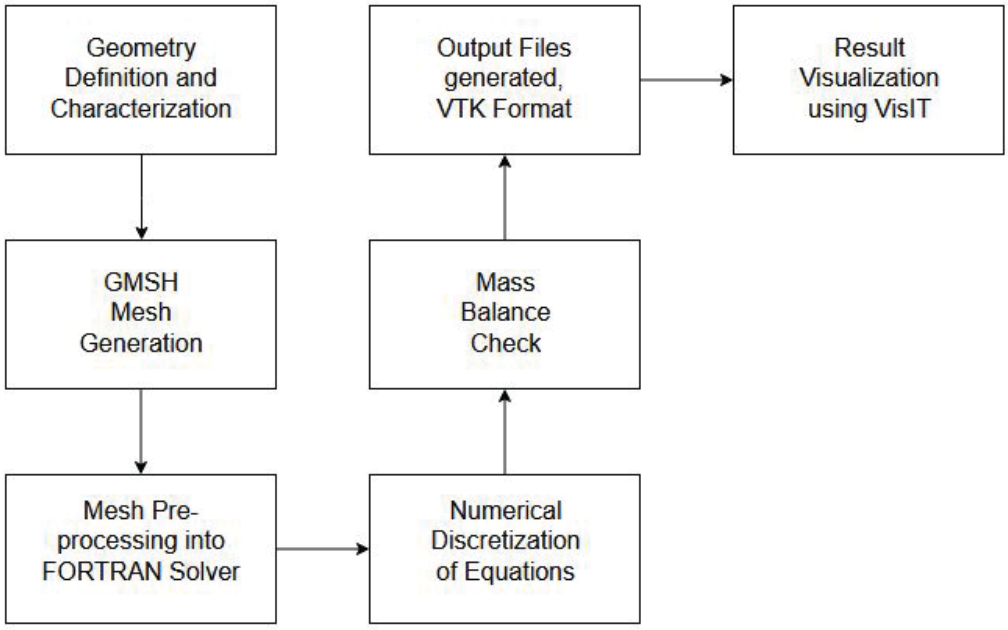

Figure 3.13 – Schematic diagram of the solution process from our developed computational framework to study flow thought shale and tight reservoirs with multi-scale fractures.

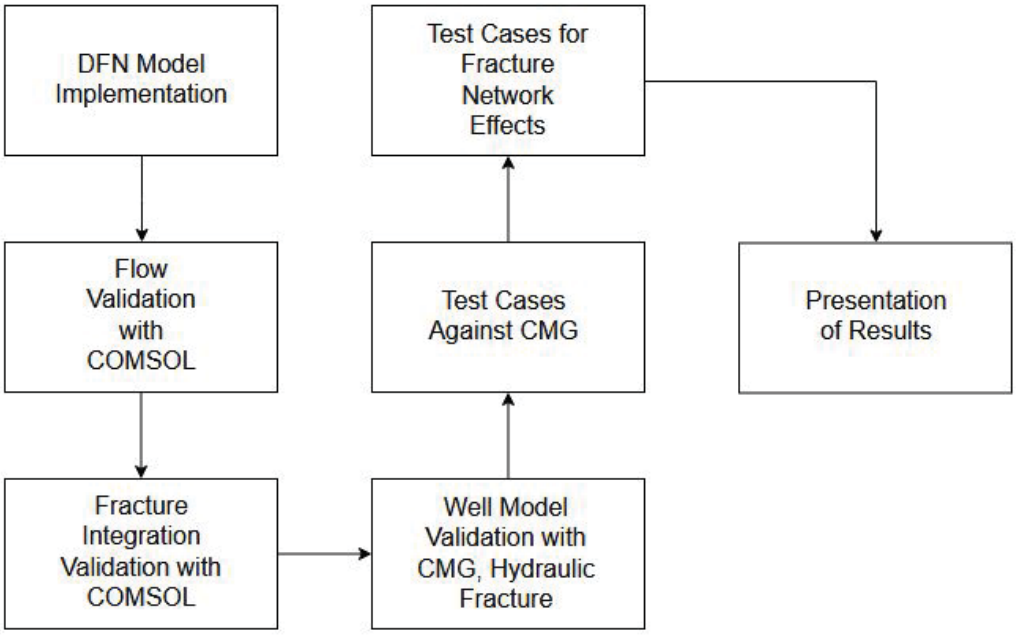

Figure 3.14 – Schematic diagram of the process followed to complete this thesis using our developed computational framework to study flow thought shale and tight reservoirs with multi-scale fractures.

Chapter 4

Results and Discussions

This chapter presents the results of the work done for the completion of this thesis. The first section describes the validation studies completed in order to demonstrate the accuracy and feasibility of the numerical model. Then, the following chapter presents the case studies where the true strength of the proposed modelling methodology is examined. Finally, the third section of this chapter presents the conclusions, relevant discussion, and final remarks of the chapter.

4.1 Model Validation

Prior to using the proposed model to evaluate and estimate oil production from unconventional, tight reservoirs; we set up a three-step validation process, each step with an increasing level of complexity.

Due to the large uncertainties linked to sub-surface flow and our lack of ability to directly corroborate by observations how the flow behaviour evolves in real formations at the field scale, validation studies play an important role to determine if the assumptions made while formulating the numerical model are in agreement with the multi physics process of transport phenomena that are know to characterize such formations and the corresponding flow patterns, and thus this process will help researchers to assess the integrity of the numerical results.

The geometry for the validation and application cases is the same rectangular domain, $200\,m$ by $500\,m$ representing a single hydraulic fracturing stage. An example of a horizontal well with two fracking stages is presented in Figure 4.1. For simplicity, we assume that a fracking stage consists of a single hydraulic fracture, although in field scale applications each fracking stage contains several hydraulic fractures, where fracture spacing optimization plays an important role in oil production. Table 4.1 presents a description of all the test cases and validation cases presented on this chapter.

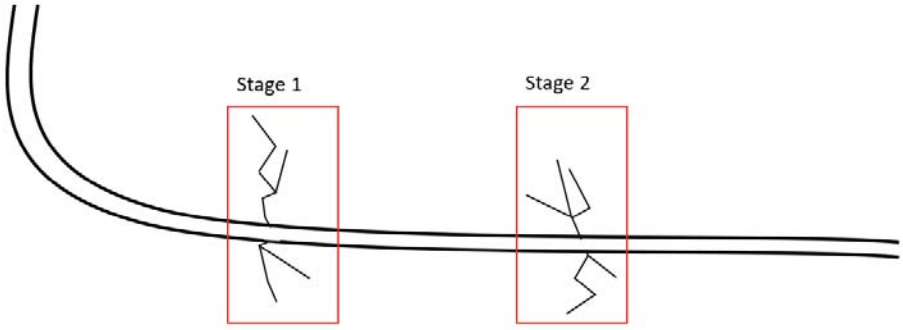

Figure 4.1 – Two-stages of hydraulic fractures on a single horizontal well.

Table 4.1 – Description of test cases and validation cases used to evaluate the proposed DFN model.

Name	Configuration	Comments
Test 01	Pressure BC, No fractures	Validated with COMSOL
Test 02	Formation stresses, No fractures	Validated with COMSOL
Test 03	DFN validation	Validated with COMSOL
Test 04	Well model validation	Validated with CMG IMEX
Application	Non-Orthogonal fractures	Parametric study

4.1.1 MFE Validation

For the first validation case, Test 01, the MFE formulation is compared with the conventional FEM for a simple pressure driven flow example on a rectangular domain. The MFE validation consists of a configuration with no fractures and each of the boundaries of a rectangular domain has a prescribed pressure value, which activates after the simulation starts at time $t = 0$; so we compare the evolution of the pressure maps and velocity fields across the whole domain.

The selected boundary conditions and relevant model setup information are shown in Table 4.2. The boundary conditions for this validation case are illustrated in Figure 4.2. The initial conditions were prescribed as:

$$\begin{aligned} p(t=0) &= 0 \\ v(t=0) &= 0 \end{aligned} \tag{4.1}$$

Table 4.2 – Transport properties for all test cases used for model validation, with appropriate references where applicable.

Property	Value	Units	Reference if applicable
Fracture compressibility	2.5×10^{-4}	psi^{-1}	[99]
Fracture permeability	1×10^{-12}	m^2	[100]
Fracture porosity	0.8	$-$	[99]
Fracture aperture	3.05×10^{-3}	m	[100–103]
Matrix compressibility	2.51×10^{-4}	psi^{-1}	[99]
Matrix permeability	1×10^{-15}	m^2	[104, 105]
Matrix porosity	0.1	$-$	[99, 105]
Oil density	900	$kg\,m^{-3}$	[106]
Oil viscosity	0.1	$Pa \cdot s$	[106]

The computational domain and pressure distribution for this configuration is shown in Figure 4.3, where the pressure distribution obtained from COMSOL is also presented. Due to the physics-controlled meshing ability of COMSOL, is not practical to show the computational mesh used in COMSOL since it will automatically use local grid refinement where pressure distributions are changing rapidly. However, from the presented results we can clearly observe the similarities between the two pressure distribution maps.

Moreover, the numerical agreement between the two solutions if further demonstrated by a cross-plot of the pressure values as a function of location, shown in Figure 4.4. The correlation coefficient between the two solutions was 0.998, and while it is very close to unity the R-squared value for the correlation may be influenced by small inaccuracies in the

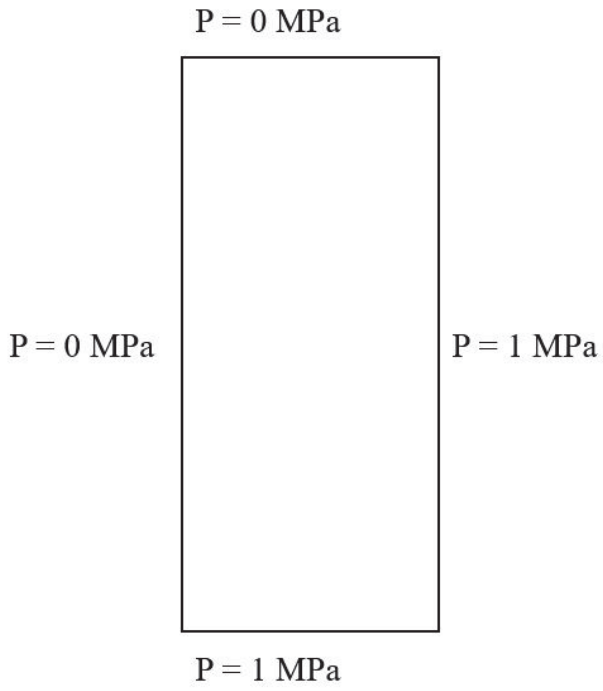

Figure 4.2 – Boundary conditions for the first MFE validation case, Test 01.

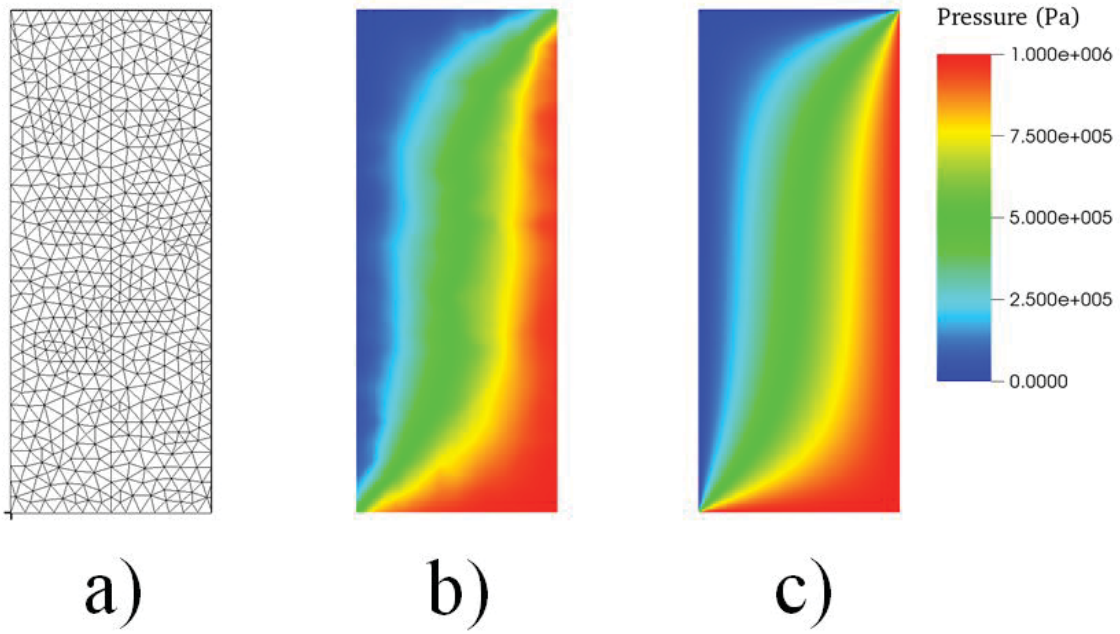

Figure 4.3 – Computational domain and flow potential map for COMSOL and our in-house MFE implementation corresponding to Test 01, unfractured reservoir. a) Computational mesh for the in-house MFE solver; b) Pressure distribution from the in-house solver; c) Pressure distribution map generated from COMSOL simulator.

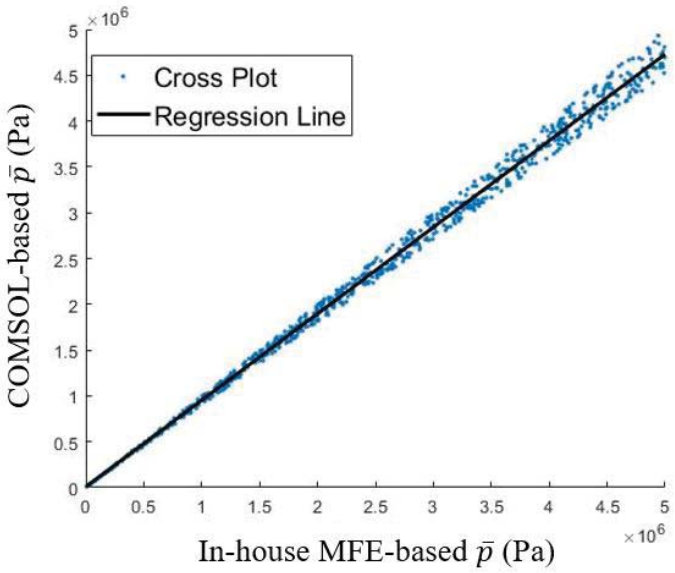

Figure 4.4 – Cross plot between COMSOL and FORTRAN for Test 01, correlation coefficient = 0.998.

locations generated from the process we used to select two matching locations based in a minimization procedure of the distance between the vertex of the COMSOL elements and the centroids of the DFN model. Additionally, COMSOL simulations are strictly incompressible, while our configuration requires a non-zero compressibility.

The computational time required to complete the simulations using out in-house Mixed Finite Element solver was nearly ten times larger than the time required by COMSOL to obtain similar solutions. Although the number of unknowns increases on a mesh of the same size when using the mixed finite elements as opposed to conventional Galerkin finite elements, COMSOL is clearly superior in terms of speed when compared to our numerical framework and solution package.

We tested a second pressure-driven configuration, Test 02, whose boundary conditions are resented in Figure 4.5. This second MFE validation case is not only intended to validate our results with COMSOL, but also to see how well the model will respond to a field-scale configuration where the tectonic stresses surrounding the reservoir are unequal. The developed framework allows to prescribe pressure boundary conditions as a function of reservoir position rather than a uniform value, but such considerations will not be taken into account for this thesis. The model parameters and configurations are presented in Table 4.2

The computational domain used for this configuration contained 800 triangular elements. The mesh, as well as the pressure maps generated from COMSOL and from our Mixed Finite Element implementation are shown in Figure 4.6. We can observe a very good agreement

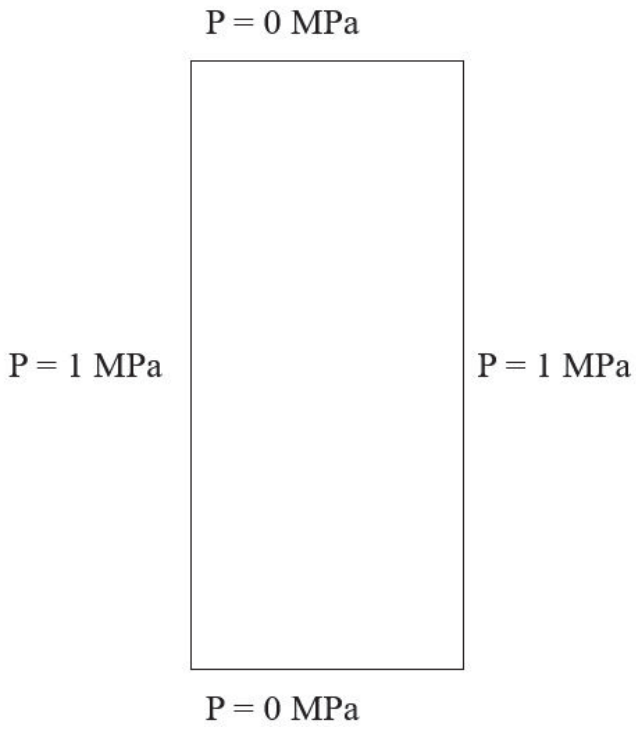

Figure 4.5 – Boundary conditions for the second MFE validation case, Test 02.

between the two numerical solutions, but the solutions generated from the implementation of the mixed finite element method is not as smooth due to mesh restrictions. While providing valid results in terms of values and predicting trends, our proposed Mixed Finite Element formulation is limited by the grid resolution when pressure values fluctuate at the boundaries. COMSOL uses local grid refinement to overcome this limitation, but our implementation lacks this capability. Smoothing of numerical solutions is not part of the scope of this project, but our proposed methodology could certainly benefit from a similar implementation.

The cross plot and regression line corresponding to this configuration, which compares the values of pressure at a specified location for both the Mixed Finite Element implementation in-house and the conventional Finite Element Method implemented with COMSOL is presented in Figure 4.7. The correlation coefficient for this configuration is 0.991, lower than that we obtained for Test 01, due to lower number of pressure level jumps. The correlation coefficient is close to unity, which reveals that the numerical results produced by our implementation is indeed in good agreement with COMSOL.

4.1.2 DFN Validation

Our testing procedure to validate the DFN formulation, referred here as Test 03, involves a direct comparison between our proposed model and an equivalent single-porosity fractured

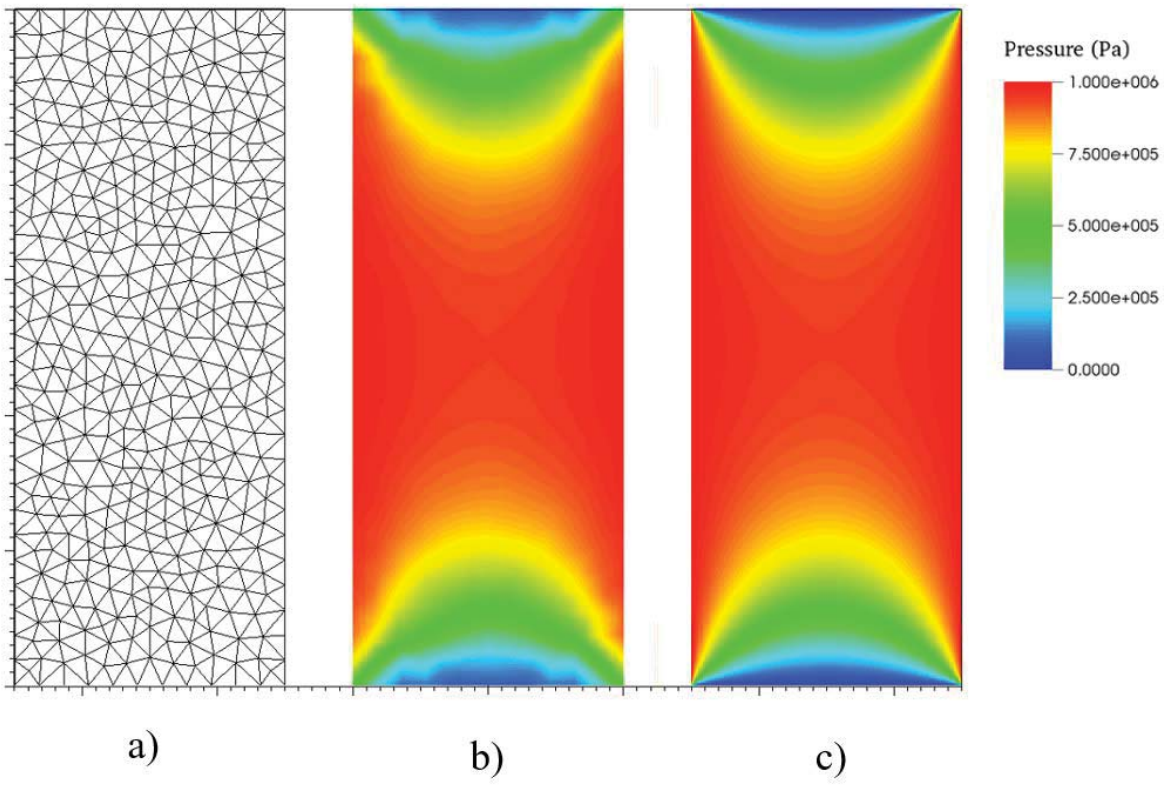

Figure 4.6 – Computational domain and flow potential map for COMSOL and our in-house MFE implementation corresponding to Test 02, unfractured reservoir. a) Computational mesh for the in-house MFE solver; b) Pressure distribution from the in-house solver; c) Pressure distribution map generated from COMSOL simulator.

model set up using COMSOL [10]. The boundary conditions for this validation case are described on Table 4.3, along with the relevant simulation parameters.

Table 4.3 – Summary table for the DFN validation case studies, using COMSOL as the benchmark.

Property	FORTRAN	COMSOL
Triangular Elements	3352	4730
Boundary Conditions	Pressure Driven Flow	Pressure Driven Flow
Total Compressibility	$2.15 \times 10^{-15}\, kPa^{-1}$	0
Matrix Porosity	0.1	0.1
Matrix Permeability	$1 \times 10^{-15} m^2$	$1 \times 10^{-15} m^2$
Fracture Porosity	0.8	0.8
Fracture Permeability	$1 \times 10^{-10} m^2$	$1 \times 10^{-10} m^2$

The computational domain and pressure maps are shown in Figure 4.8. To account for

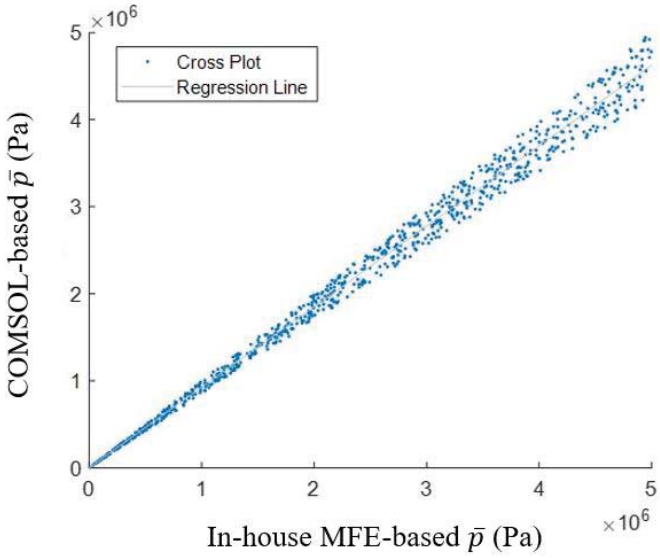

Figure 4.7 – Cross plot between COMSOL and FORTRAN for Test 02, correlation coefficient = 0.991.

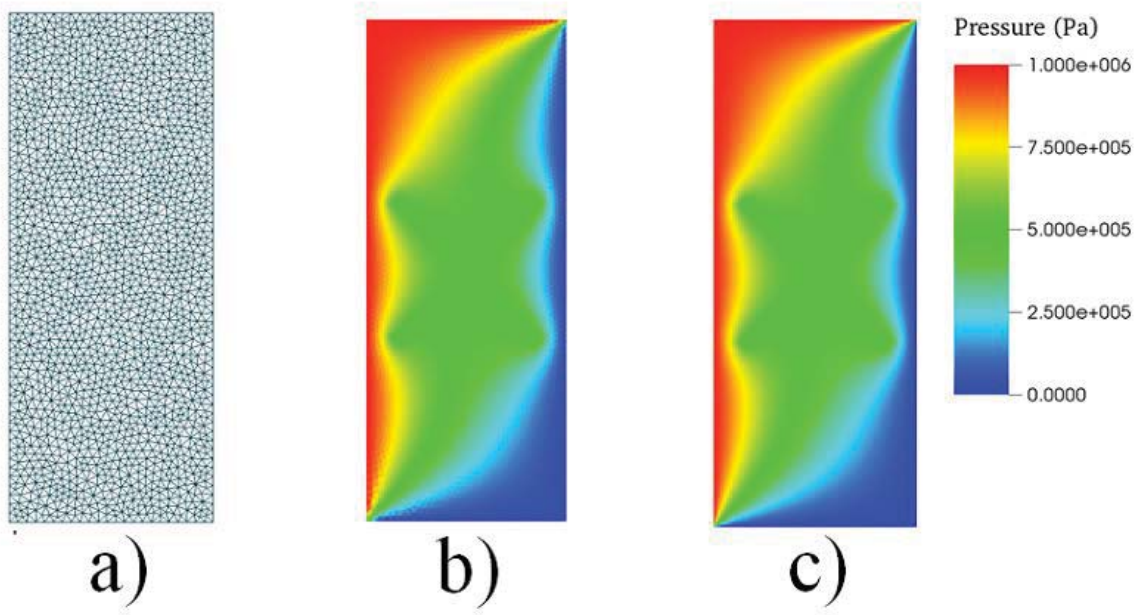

Figure 4.8 – Computational domain and flow potential map for COMSOL and our in-house MFE implementation, fractured reservoir. a) Computational mesh for the in-house MFE solver; b) Pressure distribution from the in-house solver; c) Pressure distribution map generated from COMSOL simulator.

the fact that COMSOL uses a single porosity model approach to represent fractures while our proposed model uses a DFN, we set the equivalent fracture transmissibility (the product

of fracture permeability and fracture aperture) to be the same for both configurations.

Figure 4.8 reveals that the area of impact of the fracture network is sufficiently close between the two formulations. Although some features observed in the single-porosity model cannot be observed in the discrete fracture network model, values such as average fracture pressure and velocities are in very good agreement, despite the fact that the DFN required only a fraction of the elements to generate valid solutions. With closer examination, we can still appreciate that grid resolution makes an impact on the plotting quality of the numerical solutions from our proposed Mixed Finite Element framework.

4.1.3 Well Model and Oil Production Validation

For the last validation step, Test 04, production from a tight-reservoir with a single, vertical hydraulic fracture was modelled with CMG-IMEX, [12], and compared to our implementation with point-source well models.

We used a single-porosity model approach for the CMG configurations, thus we required grid refinement. However, even with grid refinement is not practical to mesh a fracture aperture in the order of a few centimetres on a reservoir with dimensions 200 metres by 500 metres. Therefore, we used the equivalent transmissibility approach described in Section 4.1.2, where in order to mesh a fracture size ten times larger than the commonly observed values, decreasing the fracture permeability value by a tenfold will suffice. The parameters used to set up the simulation are those indicated by Table 4.2. To ensure gas is not produced, a value of $15\,kPa$ for Bubble point pressure was used, $5\,kPa$ above the initial reservoir pressure.

The mesh, pressure maps, and oil production from both configurations is shown in Figure 4.9 and Figure 4.10. The agreement difference the two production profiles is on average 12.7%, revealing that our modelling methodology can be used to study production process from fractured reservoirs.

Differences between the two production profiles can be attributed to the well models used. While our model is based on a simple, natural implementation of Darcy's law, CMG used a more elaborated and rigorous well model based on Darcy's laww as well, but taking into account radial flow from the cell where the wellbore is placed to the production or injection well; as formulated in the investigation originally published by Peaceman [9].

4.2 Case Studies

The application set-up consists on a single fracking stage, where non-orthogonal fractures are introduced by recognizing that during the fracking process the fracture propagation will fol-

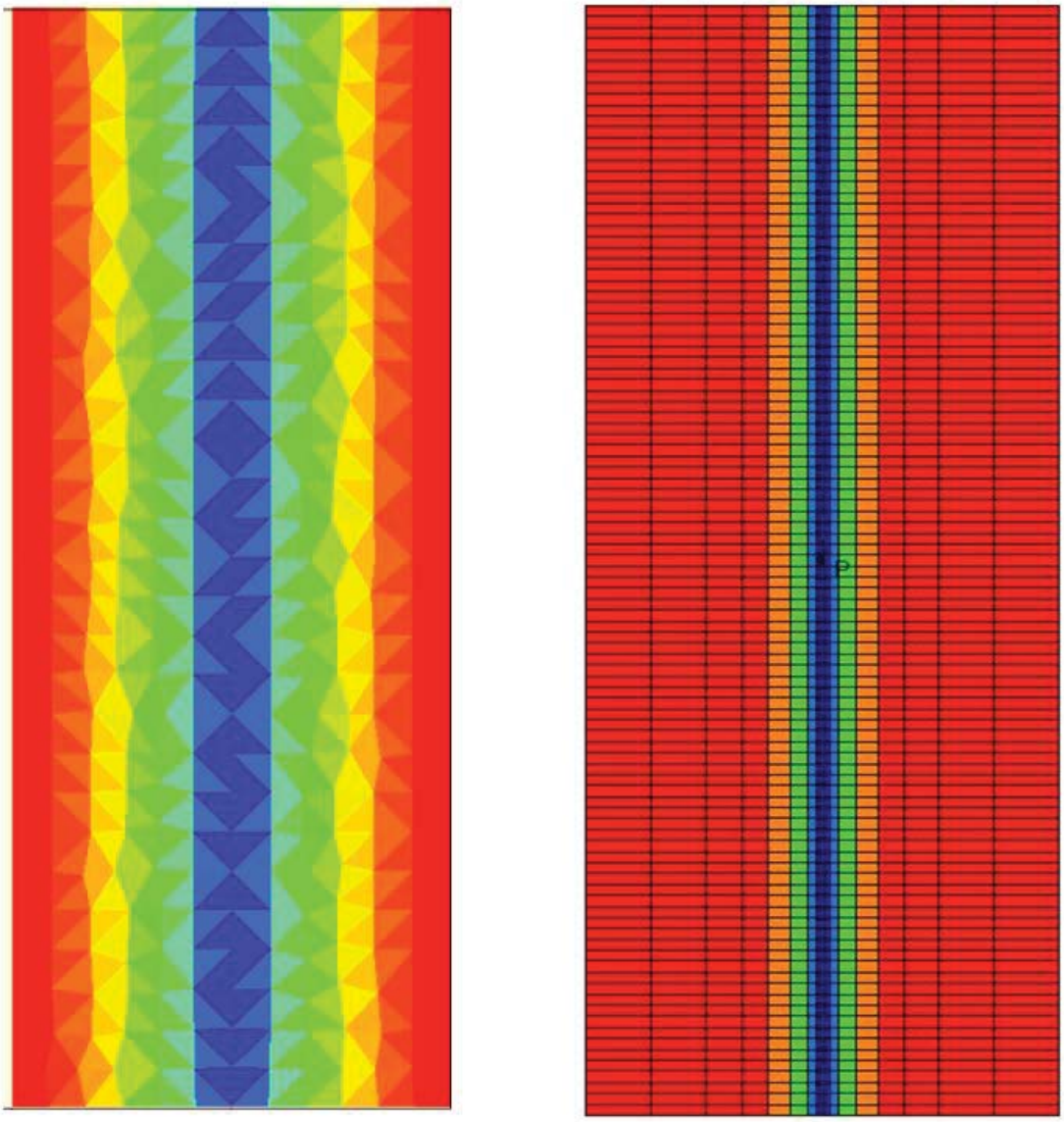

Figure 4.9 – Pressure profile comparison between the DFN model with well models using MFE implemented using FORTRAN, and CMG IMEX after 10 days.

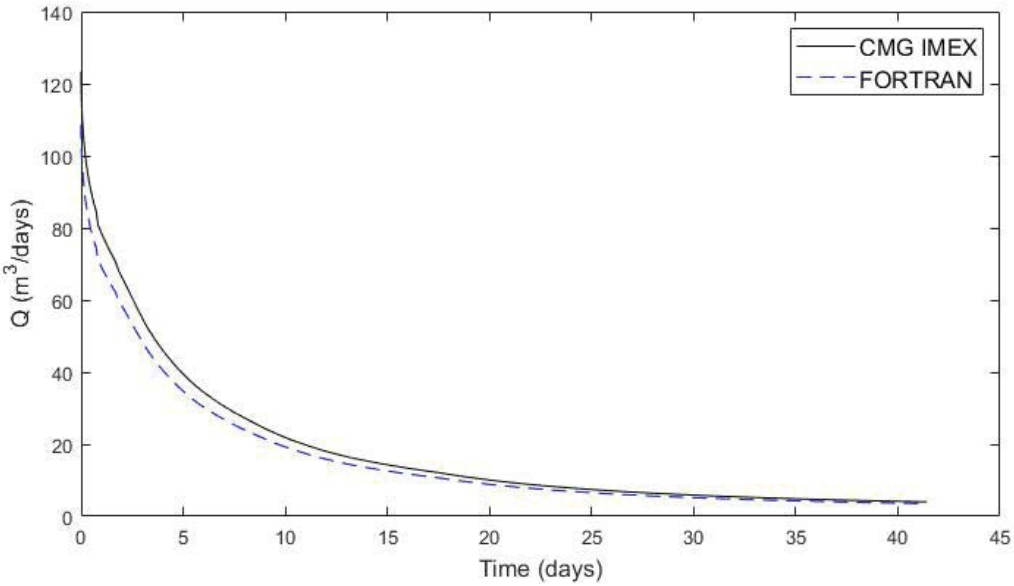

Figure 4.10 – Flow rate comparison between the DFN model with well models using MFE implemented using FORTRAN, and CMG IMEX. Production well is located at the center of the computational domain.

low an irregular pattern rather that an orthogonal, organized pattern. The effective transport properties, simulation set-up and operating conditions are the same used in Section 4.1.3. Two cases were set up to demonstrate the applicability of the proposed framework, the only difference being the fracture orientation and intensity.

The fracture distributions, computational domains and flow potential at two different times for the application cases is shown in Figure 4.11. Table 4.4 summarises the properties of the two configurations.

Table 4.4 – Summary table for the application case studies.

Property	Case A	Case B
Matrix gridcells	1141	1056
Fracture gridcells	121	86
Matrix interfaces	1678	1456
Fracture interfaces	130	90

The flow rates from the two configurations is shown in Figure 4.12, compared against the flow rate originally obtained from the validation case used in Section 4.1.3. When fracture intensity increases and they are well connected, such as the configuration shown in Case A, the production rates increase proportionally; but reservoir depletion rates are also accelerated

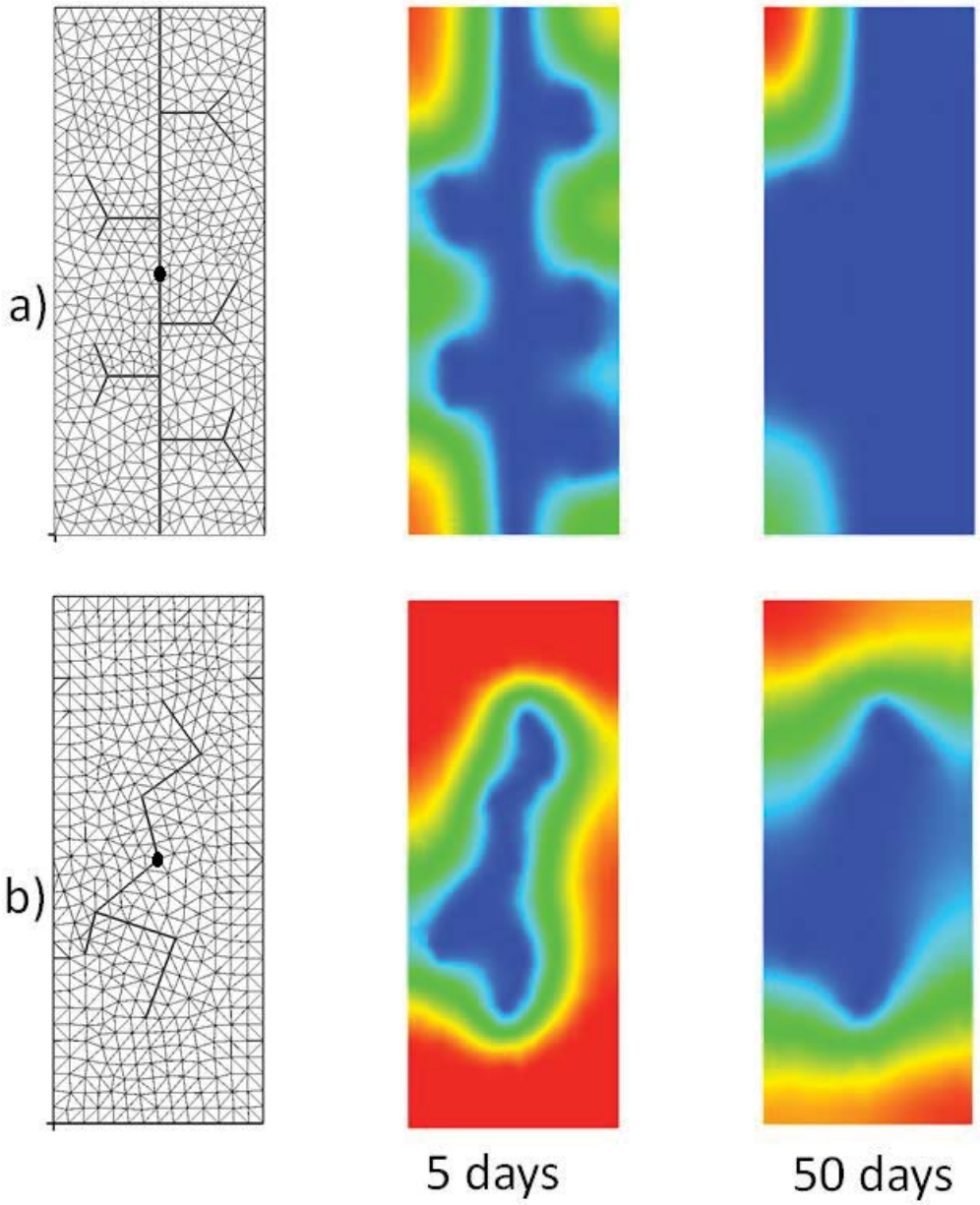

Figure 4.11 – Computational domain and flow potential for the selected application case studies, with non-orthogonal fractures. Well located at the center of the computational domain.

accordingly.

Fractures that are not very well distributed along the reservoir will display lower oil production rates, lower depletion rates, longer production times and lower performance since the reservoir pressure will not be uniform and thus some areas from the reservoir far from the fracture influence will not be produced effectively.

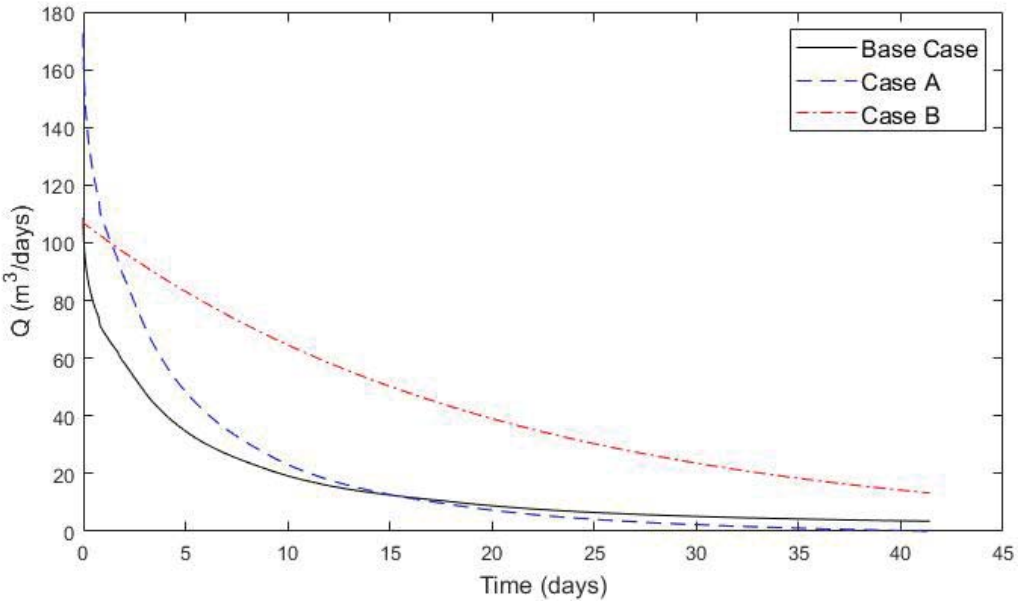

Figure 4.12 – Flow rate comparison between the DFN model with well models using MFE implemented using FORTRAN for Case A and Cased B, compared with the Base Case used in Section 4.1.3.

4.3 Effects of Fracture Aperture on Pressure Distribution

One of the most important features of the proposed modelling framework is that fractures are represented as lines in 2 dimensions, and planes in 3 dimensions in order to avoid the process of meshing them and using grid refinement as we would be required to do when modelling fracture networks using COMSOL, CMG, or any other general finite element solver.

While our proposed modelling framework allowed us to create such fracture network configurations where grid refinement is no longer a requirement for modelling, the effects of such assumptions on the pressure distribution around the fracture have not been clearly documented yet. In this section we use COMSOL to study the validity of such assumption.

We used a computational domain of $100mW \times 30mH$ and three fracture configurations: a horizontal fracture of $10m$ length located at the center of the reservoir, a vertical fracture

of $10m$ length located at the center of the reservoir, and two intersecting fractures, $10m$ length each oriented at 45 and 135^o also located at the center of the reservoir.

We used the single phase Darcy's Law solver of COMSOL to create the model, with the boundary conditions shown in Figure 4.13. The transport properties of the modelling configuration are the same used in Section 4.2. To keep the model consistent, when the fracture thickness is changed we also modify the fracture permeability, leaving the total transmissibility of the fracture network constant as detailed in Section 4.2.

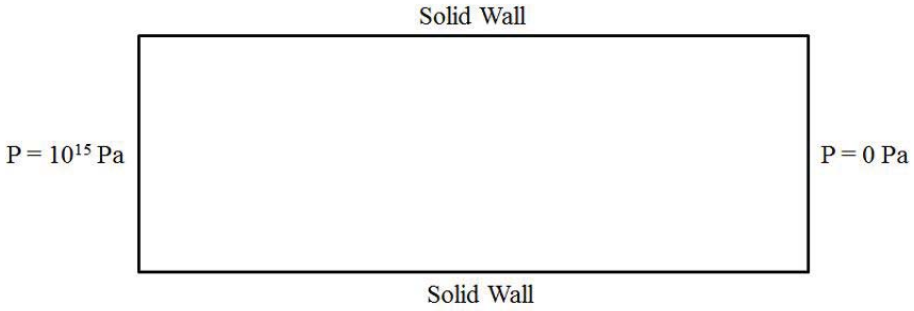

Figure 4.13 – Boundary Conditions for the tested configurations looking at the effects of fracture thickness on pressure distribution.

Pressure distribution for the three tested configurations is shown in Figure 4.14, and the pressure value at the center of the fracture for different fracture apertures is shown in Table 4.5.

As observed, the effects of fracture aperture are very minimal when the fracture orientation was crossed at angles of 45 and 135^o (Case a) and vertical (Case c). When the main fracture length was oriented along the longest pressure drop, we saw some variation of the pressure values as the aperture value decreased, because along the length of the fracture the pressure drop was the most significant out of the three configurations.

Results form this section demonstrate that the assumption of dimensionless fracture has a minor impact on pressure distribution, when the fracture length is along the direction of the largest pressure drop. However, for this tested configuration we prescribed a pressure gradient of $1 \times 10^{13}\, Pa/m$, which is quite significant in order to better quantify the possible effects of fracture orientation. Under normal operating conditions, such pressure drops are not very common. Therefore, even with minor effects on pressure distribution, the assumption of aperture-less fractures does not invalidate the numerical results.

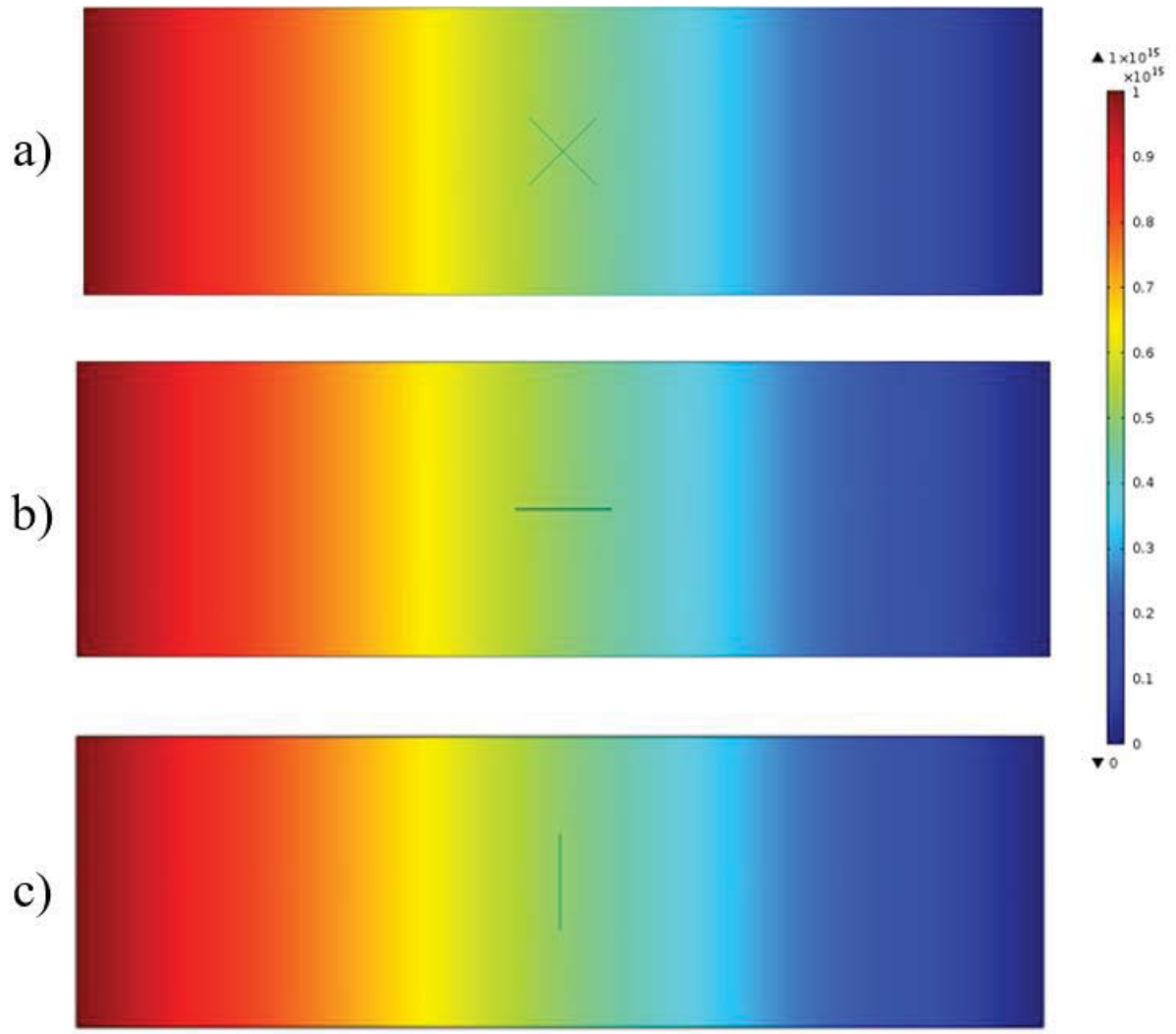

Figure 4.14 – Pressure distribution maps for the tested configurations looking at the effects of fracture thickness.

Table 4.5 – Summary table for pressure values as a function of fracture aperture.

Fracture Aperture	Pressure Case a)	Pressure Case b)	Pressure Case c)
3.2m	$4.999\,10^{14}\,Pa$	$5.001\,10^{14}\,Pa$	$5.000\,10^{14}\,Pa$
1.6m	$5.000\,10^{14}\,Pa$	$5.003\,10^{14}\,Pa$	$5.000\,10^{14}\,Pa$
0.8m	$4.999\,10^{14}\,Pa$	$5.006\,10^{14}\,Pa$	$5.000\,10^{14}\,Pa$
0.4m	$5.000\,10^{14}\,Pa$	$5.011\,10^{14}\,Pa$	$5.000\,10^{14}\,Pa$
0.2m	$5.000\,10^{14}\,Pa$	$5.020\,10^{14}\,Pa$	$5.000\,10^{14}\,Pa$
0.1m	$5.000\,10^{14}\,Pa$	$5.037\,10^{14}\,Pa$	$5.000\,10^{14}\,Pa$
0.05m	$5.000\,10^{14}\,Pa$	$5.068\,10^{14}\,Pa$	$5.000\,10^{14}\,Pa$
0.025m	$5.000\,10^{14}\,Pa$	$5.117\,10^{14}\,Pa$	$5.000\,10^{14}\,Pa$
0.0125m	$5.000\,10^{14}\,Pa$	$5.187\,10^{14}\,Pa$	$5.000\,10^{14}\,Pa$
0.00625m	$5.000\,10^{14}\,Pa$	$5.267\,10^{14}\,Pa$	$5.000\,10^{14}\,Pa$
0.003125m	$5.000\,10^{14}\,Pa$	$5.343\,10^{14}\,Pa$	$5.000\,10^{14}\,Pa$
0.001563m	$5.000\,10^{14}\,Pa$	$5.401\,10^{14}\,Pa$	$5.000\,10^{14}\,Pa$
0.000781m	$5.000\,10^{14}\,Pa$	$5.441\,10^{14}\,Pa$	$5.000\,10^{14}\,Pa$

4.4 Discussion and Final Remarks

The results obtained at the end of this Chapter are very encouraging. In the past, the Mixed Finite Element method has been proven to be a great modelling alternative to study flow through fracture reservoirs, but the scope of most studies was not focus on tight and shale formations, and the numerical solutions of the oil production process is still at an early stage of exploration.

Our model demonstrated to be a robust alternative to the conventional Finite Element Method, and predicted results from simple configurations with no fractures compared favourably with COMSOL. With complex pressure boundary conditions, where pressure values jump at adjacent edges, the inability of our model to automatically perform local grid refinement put it at a slight disadvantage when comparing it to COMSOL. However, as the results generated from CMG IMEX revealed, such features are not implemented on some of the commercial oil simulators either. Other factor where COMSOL was superior to our developed Mixed Finite Element framework was computational time required to generate valid numerical solutions, where solution time increased by almost a tenfold when compared to the time required to generate solutions using COMSOL.

When compared to CMG IMEX with a single, orthogonal hydraulic fracture, our computational framework underpredicted oil production rates by approximately 10%. The reason for this discrepancy is attributed to:

- The well model, which underpredicts oil production rates by 8% for a simple configu-

ration with a vertical hydraulic fracture oriented at 90^o.

- Model accuracy, since for similar sized meshes, the mixed finite element method is more accurate than the numerical schemes implemented in CMG IMEX.

Moreover, our model revealed that the fracture pressure when the hydraulic fractures are well connected is almost constant, so there is minimum pressure drop inside well connected fracture networks.

Furthermore, when fractures are well connected oil production is directly proportional to the hydraulic fracture volume, and reservoir depletion takes place at a much longer time when the fracture network is small and does not extend to the reservoir boundaries to promote a sustainable pressure drop. This is under the assumptions that the fracture stage is isolated and that if multiple fracking stages exists, they are far enough that they do not exert any influence to other fracking stages.

Chapter 5

Conclusions, Final Remarks and Future Work

In this chapter, we present our final conclusions and remarks. Also, we revisit the contributions made by the end of this thesis, and outline the directions for future work as a continuation of this work.

5.1 Conclusions

After finishing these studies, we verified that the Mixed Finite Element Method is a great alternative to perform numerical simulation of sub-surface flow, offering many advantages and none of the shortcomings of other numerical schemes such as the conventional Finite Element Method and the control Volume method, other than the increase in the number of unknowns, but this is partially alleviated by the direct computation of pressure and fluxes values, rather than involving an additional step and solving two systems of equations separately. Our validation studies demonstrated that pressure maps generated from the Mixed Finite Element Method are as accurate as pressure maps generated from COMSOL, a well established multi-physics package based on the conventional Finite Element Method.

Additionally, our studies demonstrated that fracture connectivity plays a key role in production performance from ultra-low permeability fractured rock formations. In test studies, reservoirs with fractures not connected to the network that feeds the well displayed almost identical production profiles than configurations where such disconnected fractures were removed; thus reinforcing the hypothesis that while some fractures are key factors on reservoir performance we must be accurately depicted discretely for results and predictions to be fully representative, other fractures can be excluded from the model and still prediction and results' integrity is maintained.

5.2 Contributions of this Thesis

With the culmination of this thesis, we proposed a methodology to look at unconventional rock formations with natural and hydraulic fractures. Fractures are discretely represented, but using lower dimensions for their physical presence in the computational domain allows for efficient grids without the need of extensive grid refinement due to the differences in spatial scales. The model is flexible enough to allow the integration of different fracture networks with different properties, thus allowing researchers to look at natural and hydraulic fractures with the same model, at the same time, and capturing the interaction between the two fracture networks.

A point-source well model was incorporated, thus we are able to study the production process from ultra-low permeability formations. The formulation of the model is well outlined, and based on a conventional implementation of the Mixed Finite Element Method, where pressure values are evaluated at the center of triangular elements, and pressure gradients (velocities or fluxes) are evaluated the the boundaries of the triangular elements. The utilization of the Mixed Finite Element Method ensures that the methodology we followed enforces mass conservation both locally and globally, thus being a more robust alternative in this aspect that methodologies based on the conventional Finite Element method, Finite Volume method, Control Volume-Based methods with two point or multi point flux approximations, and the Finite Difference method.

The implemented mesh generation approach worked very well to represent fractures as a lower-dimensional physical entity in the physical domain. For all test cases and case studies considered, the Delaunay triangulation meshing technique generated robust meshes with seamless fracture integration.

5.3 Directions for Future Work

Future work for the presented DFN formulation should incorporate the multi-phase aspect of flow through tight, fractured reservoirs. Black oil simulators often can be considered as the foundation for more complex, elaborated models. Extending the presented model to two or three phases will provide additional insight to the behaviour of naturally and hydraulic fractured unconventional reservoirs.

Due to the difference in scales, well models are often the link between reservoir behaviour, reservoir pressure distribution, and reservoir performance. Therefore, additional research can be completed regarding the utilization of more advanced well models for production from fractured, unconventional reservoirs. With the model implemented on this thesis, point-source well models are simple to implement yet effective at describing oil production, but

other options can definitely be considered.

Furthermore, for rock formations where the permeability is ultra-low, such as tight shale formations, where formation pressures are high, the fracking process will create ultra-high conductivity conduits for the flow to be produced. Due to the small spacial dimensions of the fractures and the high flow rates one might encounter, the validity of Darcy's law, which ignores the effects of turbulent flow, might be questionable.

The present methodology is hindered by the computational time required to compute numerical solutions. This work would also benefit from additional research into parallel computing and efficient solutions for linear systems of equations where the stiffness matrix is not symmetric.

Finally, the continuation of this project would benefit tremendously if the proposed methodology is coupled with a complete procedure to perform upscaling analysis; which is one of the preferred techniques to acknowledge that there is certain amount of uncertainty in such sub-surface flow model due to the inability to accurately describe the geomorphology of the formations, and at the same time introduce the uncertainty back into the simulations by providing a normalized distribution rather than a single value for the oil production profiles. Moreover, upscaling can also be used to create a framework to determine at which point is more feasible to remove fractures out of the model if their overall impact on production performance is not significant, based on fracture orientation, fracture density, fracture connectivity, and distance from the production well.

References

[1] Office of fossil energy. shale gas 101. https://www.energy.gov/fe/shale-gas-101, . Accessed: 2019-05-30.

[2] Office of fossil energy. shale gas 101, why is shale gas important? https://www.energy.gov/sites/prod/files/2013/04/f0/why_is_shale_gas_important.pdf, . Accessed: 2019-05-30.

[3] J Chong and M. Simikian. Shale gas in canada: Resource potential, current production and economic implications. *Library of the Parliament*, 01 2014. URL https://lop.parl.ca/staticfiles/PublicWebsite/Home/ResearchPublications/InBriefs/PDF/2014-08-e.pdf.

[4] George E. King and Danny Durham. Chapter one - hydraulic fracturing: The technology explained. In Kevin A. Schug and Zacariah L. Hildenbrand, editors, *Environmental Issues Concerning Hydraulic Fracturing*, volume 1 of *Advances in Chemical Pollution, Environmental Management and Protection*, pages 1 – 16. Elsevier, 2017. doi: https://doi.org/10.1016/bs.apmp.2017.08.005. URL http://www.sciencedirect.com/science/article/pii/S2468928917300059.

[5] Office of fossil energy. natural gas from shale: Questions and answers. https://www.energy.gov/sites/prod/files/2013/04/f0/complete_brochure.pdf, . Accessed: 2019-05-30.

[6] Scientific american. water use rises as fracking expands. https://www.scientificamerican.com/article/water-use-rises-as-fracking-expands/. Accessed: 2019-05-30.

[7] Scott Jasechko and Debra Perrone. Hydraulic fracturing near domestic groundwater wells. *Proceedings of the National Academy of Sciences*, 114(50):13138–13143, 2017. ISSN 0027-8424. doi: 10.1073/pnas.1701682114. URL https://www.pnas.org/content/114/50/13138.

[8] Honn Kao, Roy Hyndman, Yan Jiang, Ryan Visser, Brindley Smith, Alireza Babaie Mahani, Lucinda Leonard, Hadi Ghofrani, and Jiangheng He. Induced seismicity in western canada linked to tectonic strain rate: Implications for regional seismic hazard. *Geophysical Research Letters*, 45(20):11,104–11,115, 2018. doi: 10.1029/2018GL079288. URL `https://agupubs.onlinelibrary.wiley.com/doi/abs/10.1029/2018GL079288`.

[9] D. W. Peaceman. Interpretation of well-block pressures in numerical reservoir simulation. *SPE Journal*, 18(3):183 – 194, 1978.

[10] COMSOL Inc. COMSOL Multiphysics. `http://www.comsol.com/`, 2019. Accessed: 2019-02-02.

[11] Computer Modelling Group LTD. CMG. `http://www.cmgl.ca/`, 2019. Accessed: 2019-02-02.

[12] Computer Modelling Group LTD. CMG IMEX. `https://www.cmgl.ca/imex`, 2019. Accessed: 2019-23-02.

[13] Schlumberger Limited. INTERSECT High-Resolution Reservoir Simulator. `https://www.software.slb.com/products/intersect`, 2019. Accessed: 2019-23-02.

[14] Jorge Eduardo Palomino Monteagudo, Adolfo Antonio Rodriguez, and Horacio Florez. Simulation of flow in discrete deformable fractured porous media. In *SPE Reservoir Simulation Symposium 2011*, pages 1–16. Society of Petroleum Engineers, February 2011.

[15] Stein Krogstad, Knut, Andreas E. Lie, Olav Møyner, Halvor Møll Nilsen, and Xavier Raynaud. Mrst-ad - an open-source framework for rapid prototyping and evaluation of reservoir simulation problems. In *ANSS 2015*, 2015.

[16] Hussein Hoteit and Abbas Firoozabadi. Compositional Modeling of Discrete-Fractured Media Without Transfer Functions by the Discontinuous Galerkin and Mixed Methods. *SPE Journal*, 11(3):341 – 352, 2006.

[17] Hussein Hoteit and Abbas Firoozabadi. An efficient numerical model for incompressible two-phase flow in fractured media. *Advances in Water Resources*, 31(6):891–905, 2008.

[18] W. Narr, D.S. Schechter, and L.B. Thompson. *Naturally Fractured Reservoir Characterization*. An interdisciplinary approach to topics in petroleum engineering and geosciences. Society of Petroleum Engineers, 2006. ISBN 9781555631123. URL `https://books.google.ca/books?id=aF15MwAACAAJ`.

[19] Younes Fadakar Alghalandis. Adfne: Open source software for discrete fracture network engineering, two and three dimensional applications. *Computers & Geosciences*, 102:1 – 11, 2017. ISSN 0098-3004. doi: https://doi.org/10.1016/j.cageo.2017.02.002.

[20] Xia Yan, Zhaoqin Huang, Jun Yao, Yang Li, and Dongyan Fan. An efficient embedded discrete fracture model based on mimetic finite difference method. *Journal of Petroleum Science and Engineering*, 145:11 – 21, 2016. ISSN 0920-4105. doi: https://doi.org/10.1016/j.petrol.2016.03.013.

[21] Qingfu Zhang, Zhaoqin Huang, Jun Yao, Yueying Wang, and Yang Li. Multiscale mimetic method for two-phase flow in fractured media using embedded discrete fracture model. *Advances in Water Resources*, 107:180 – 190, 2017. ISSN 0309-1708. doi: https://doi.org/10.1016/j.advwatres.2017.06.020.

[22] Wei Liu and Yirang Yuan. Finite difference schemes for two-dimensional miscible displacement flow in porous media on composite triangular grids. *Computers & Mathematics with Applications*, 55(3):470 – 484, 2008. ISSN 0898-1221. doi: https://doi.org/10.1016/j.camwa.2007.05.003.

[23] David W. Zingg and Harvard Lomax. Finite-difference schemes on regular triangular grids. *J. Comput. Phys.*, 108(2):306–313, October 1993. ISSN 0021-9991. doi: 10.1006/jcph.1993.1184.

[24] Changfeng Li and Yirang Yuan. Domain decomposition with characteristic finite difference method for two-phase displacement problems. *Applied Numerical Mathematics*, 58(9):1262 – 1273, 2008. ISSN 0168-9274. doi: https://doi.org/10.1016/j.apnum.2007.07.006.

[25] Jim Douglas, Jeffrey L. Hensley, and Todd Arbogast. A dual-porosity model for waterflooding in naturally fractured reservoirs. *Computer Methods in Applied Mechanics and Engineering*, 87(2):157 – 174, 1991. ISSN 0045-7825. doi: https://doi.org/10.1016/0045-7825(91)90004-P.

[26] James H. Bramble and Miloš Zlámal. Triangular elements in the finite element method. *Mathematics of Computation*, 24(112):809–820, 1970. ISSN 00255718, 10886842. URL `http://www.jstor.org/stable/2004615`.

[27] O.C. Zienkiewicz, R.L. Taylor, and J.Z. Zhu. *The Finite Element Method: Its Basis and Fundamentals*. Butterworth-Heinemann, 7 edition, 2013.

[28] Youshi Jiang and Arash Dahi Taleghani. Modified extended finite element methods for gas flow in fractured reservoirs: A pseudo-pressure approach. *Journal of Solar Energy Engineering, Transactions of the ASME*, 140(7), 7 2018. ISSN 0199-6231. doi: 10.1115/1.4039327.

[29] Guy Chavent and Jerome Jaffre. Chapter i basic laws and models for flow in porous media. In *Mathematical Models and Finite Elements for Reservoir Simulation Single Phase, Multiphase and Multicomponent Flows through Porous Media*, volume 17 of *Studies in Mathematics and Its Applications*, pages 1 – 50. Elsevier, 1986. doi: http://dx.doi.org/10.1016/S0168-2024(08)70079-1. URL `http://www.sciencedirect.com/science/article/pii/S0168202408700791`.

[30] Guy Chavent and Jerome Jaffre. Chapter v: A finite element method for incompressible two-phase flow. In *Mathematical Models and Finite Elements for Reservoir Simulation Single Phase, Multiphase and Multicomponent Flows through Porous Media*, volume 17 of *Studies in Mathematics and Its Applications*, pages 311 – 364. Elsevier, 1986. doi: http://dx.doi.org/10.1016/S0168-2024(08)70083-3. URL `http://www.sciencedirect.com/science/article/pii/S0168202408700833`.

[31] Jahan Noorishad and Mohsen Mehran. An upstream finite element method for solution of transient transport equation in fractured porous media. *Water Resources Research*, 18(3):588–596, 1982. doi: 10.1029/WR018i003p00588.

[32] X. Yan, Z. Huang, J. Yao, Y. Li, D. Fan, H. Sun, and K. Zhang. An efficient numerical hybrid model for multiphase flow in deformable fractured-shale reservoirs. *Society of Petroleum Engineers Journal*, 23(4):1412 – 1437, 2018. doi: https://doi.org/10.2118/191122-PA.

[33] L. Mi, C. An, Y. Cao, B. Yan, H. Jiang, Y. Pei, and J.E. Killough. A guideline on optimizing fracture modeling for fractured reservoir simulation. In *2016 SPE Asia Pacific Hydraulic Fracturing Conference*, pages 1 – 17. Society of Petroleum Engineers. doi: https://doi.org/10.2118/181814-MS.

[34] Louis J. Durlofsky. A triangle based mixed finite element—finite volume technique for modeling two phase flow through porous media. *Journal of Computational Physics*, 105 (2):252 – 266, 1993. ISSN 0021-9991. doi: http://dx.doi.org/10.1006/jcph.1993.1072. URL `http://www.sciencedirect.com/science/article/pii/S0021999183710727`.

[35] R. A. Klausen and T. F. Russell. Relationships among some locally conservative discretization methods which handle discontinuous coefficients. *Computational Geosciences*, 8(4):341–377, Dec 2004. ISSN 1573-1499. doi: 10.1007/s10596-005-1815-9.

[36] Y. Fu, Y. K. Yang, and M. Deo. Three-dimensional, three-phase discrete-fracture reservoir simulator based on control volume finite element (cvfe) formulation. In *2005 SPE Reservoir Simulation Symposium*. Society of Petroleum Engineers, jan-feb 2005. ISBN 978-1-61399-010-0. doi: 10.2118/93292-MS.

[37] J. E. P. Monteagudo and A. Firoozabadi. Comparison of fully implicit and impes formulations for simulation of water injection in fractured and unfractured media. *International Journal for Numerical Methods in Engineering*, 69(4):698–728, 2007. URL `http://dx.doi.org/10.1002/nme.1783`.

[38] J. E. P. Monteagudo and A. Firoozabadi. Control-volume model for simulation of water injection in fractured media: incorporating matrix heterogeneity and reservoir wettability effects. *SPE Journal*, 12(3):355–366, 2007.

[39] J. E. P. Monteagudo and A. Firoozabadi. Control-volume method for numerical simulation of two-phase immiscible flow in two- and three-dimensional discrete-fractured media. *Water Resources Research*, 40(7):W07405, 2004. URL `http://dx.doi.org/10.1029/2003WR002996`.

[40] T. H. Sandve, I. Berre, and J. M. Nordbotten. An efficient multi-point flux approximation method for discrete fracture-matrix simulations. *Journal of Computational Physics*, 231(9):3784–800, 05/01 2012. URL `http://dx.doi.org/10.1016/j.jcp.2012.01.023`. undefined; undefined; undefined; undefined; undefined; undefined; undefined; undefined; undefined.

[41] Vaughan R Voller. *Basic Control Volume Finite Element Methods for Fluids and Solids*. World Scientific Publishing Co. Pte. Ltd., 1 edition, 2009.

[42] Ivar Aavatsmark. An introduction to multipoint flux approximations for quadrilateral grids. *Computational Geosciences*, 6(3):405–432, Sep 2002. ISSN 1573-1499. doi: 10.1023/A:1021291114475. URL `https://doi.org/10.1023/A:1021291114475`.

[43] Q.-Y. Chen, R. T. Mifflin, J. Wan, and Y Yang. A new multipoint flux approximation for reservoir simulation. In *2007 SPE Reservoir Simulation Symposium*, pages 1 – 9. Society of Petroleum Engineers. doi: https://doi.org/10.2118/106464-MS.

[44] Franco Brezzi and Michel Fortin. *Mixed and Hybrid Finite Element Methods*, volume 15 of *Springer Series in Computational Mathematics*. Springer-Verlag New York, 1 edition, 3 1991.

[45] Franco Brezzi, Jim Douglas, and L. D. Marini. Two families of mixed finite elements for second order elliptic problems. *Numerische Mathematik*, 47(2):217–235, Jun 1985. ISSN 0945-3245. doi: 10.1007/BF01389710.

[46] P.A. Raviart and J.M. Thomas. A mixed hybrid finite element method for the second order elliptic problem. Lecture notes in mathematics, 1977.

[47] P A. Raviart and J M. Thomas. *A Mixed Finite Element Method for Second Order Elliptic Problems*, volume 606. 11 2006. doi: 10.1007/BFb0064470.

[48] Jiangguo Liu, Lin Mu, and Xiu Ye. A comparative study of locally conservative numerical methods for darcy's flows. *Procedia Computer Science*, 4:974 – 983, 2011. ISSN 1877-0509. doi: https://doi.org/10.1016/j.procs.2011.04.103. Proceedings of the International Conference on Computational Science, ICCS 2011.

[49] M. Vohralík, J. Maryška, and O. Severýn. Mixed and nonconforming finite element methods on a system of polygons. *Applied Numerical Mathematics*, 57(2):176 – 193, 2007. ISSN 0168-9274. doi: https://doi.org/10.1016/j.apnum.2006.02.005.

[50] Najla Frih, Vincent Martin, JeanElizabeth Roberts, and Ali Saâda. Modeling fractures as interfaces with nonmatching grids. *Computational Geosciences*, 16(4):1043–1060, 2012. ISSN 1420-0597. doi: 10.1007/s10596-012-9302-6.

[51] Arif Masud and Thomas J.R. Hughes. A stabilized mixed finite element method for darcy flow. *Computer Methods in Applied Mechanics and Engineering*, 191(39–40):4341 – 4370, 2002. ISSN 0045-7825. doi: http://dx.doi.org/10.1016/S0045-7825(02)00371-7. URL `http://www.sciencedirect.com/science/article/pii/S0045782502003717`.

[52] Thomas J.R. Hughes, Arif Masud, and Jing Wan. A stabilized mixed discontinuous galerkin method for darcy flow. *Computer Methods in Applied Mechanics and Engineering*, 195(25–28):3347 – 3381, 2006. ISSN 0045-7825. doi: http://dx.doi.org/10.1016/j.cma.2005.06.018. URL `http://www.sciencedirect.com/science/article/pii/S0045782505002732`. Discontinuous Galerkin Methods.

[53] Hussein Hoteit and Abbas Firoozabadi. Compositional Modeling by the Combined Discontinuous Galerkin and Mixed Methods. *SPE Journal*, 11(1):19 – 34, 2006.

[54] Hussein Hoteit and Abbas Firoozabadi. Numerical modeling of two-phase flow in heterogeneous permeable media with different capillarity pressures. *Advances in Water Resources*, 31(1):56 – 73, 2008. ISSN 0309-1708. doi: http://dx.doi.org/10.1016/

j.advwatres.2007.06.006. URL http://www.sciencedirect.com/science/article/pii/S030917080700108X.

[55] Radek Fučík and Jiří Mikyška. Discontinous galerkin and mixed-hybrid finite element approach to two-phase flow in heterogeneous porous media with different capillary pressures. *Procedia Computer Science*, 4(0):908 – 917, 2011. ISSN 1877-0509. doi: http://dx.doi.org/10.1016/j.procs.2011.04.096. URL http://www.sciencedirect.com/science/article/pii/S1877050911001542. ¡ce:title¿Proceedings of the International Conference on Computational Science, {ICCS} 2011¡/ce:title¿.

[56] H. Hoteit and A. Firoozabadi. Multicomponent fluid flow by discontinuous galerkin and mixed methods in unfractured and fractured media. *Water Resources Research*, 41(11):n/a–n/a, 2005. ISSN 1944-7973. doi: 10.1029/2005WR004339. URL http://dx.doi.org/10.1029/2005WR004339. W11412.

[57] Jiří Maryška, Otto Severýn, and Martin Vohralík. Numerical simulation of fracture flow with a mixed-hybrid fem stochastic discrete fracture network model. *Computational Geosciences*, 8(3):217–234, Jan 2005. ISSN 1573-1499. doi: 10.1007/s10596-005-0152-3.

[58] Jiří Maryška, Miroslav Rozložník, and Miroslav Tůma. Primal vs. dual variable approach for mixed-hybrid finite element approximation of the potential fluid flow problem in porous media. In Svetozar Margenov, Jerzy Waśniewski, and Plamen Yalamov, editors, *Large-Scale Scientific Computing*, pages 417–424, Berlin, Heidelberg, 2001. Springer Berlin Heidelberg. ISBN 978-3-540-45346-8.

[59] M. Vohralík, J. Maryška, and O. Severýn. Mixed and nonconforming finite element methods on a system of polygons. *Appl. Numer. Math.*, 57(2):176–193, February 2007. ISSN 0168-9274. doi: 10.1016/j.apnum.2006.02.005. URL http://dx.doi.org/10.1016/j.apnum.2006.02.005.

[60] Pavel Tomin and Anna Pergament. Single porosity model for fractured formations. In *ECMOR 2012 - 13th European Conference on the Mathematics of Oil Recovery*, pages 1 – 13, 09 2012. doi: 10.3997/2214-4609.20143169.

[61] R Abdel-Ghani. Single porosity simulation of fractures with low to medium fracture to matrix permeability contrast. *Society of Petroleum Engineers*, 01 2009. doi: 10.2118/125565-MS.

[62] K Ghorayeb and A Firoozabadi. Numerical study of natural convection and diffusion in fractured porous media. *Society of Petroleum Engineers*, 5(1):12 – 20, 03 2000. doi: doi:10.2118/51347-PA.

[63] G.I Barenblatt, Iu.P Zheltov, and I.N Kochina. Basic concepts in the theory of seepage of homogeneous liquids in fissured rocks [strata]. *Journal of Applied Mathematics and Mechanics*, 24(5):1286 – 1303, 1960. ISSN 0021-8928. doi: https://doi.org/10.1016/0021-8928(60)90107-6.

[64] T. W. Doe, M. Uchida, J. S. Kindred, and W. S. Dershowitz. Simulation of dual-porosity flow in discrete fracture networks. In *Annual Technical Meeting 1990*, pages 1 – 8. Petroleum Society of Canada, 01 1990. doi: 10.2118/90-120.

[65] J. E. Warren and P. J. Root. The behavior of naturally fractured reservoirs. *Society of Petroleum Engineers*, 3(3):245 – 255, 09 1963. doi: doi.org/10.2118/426-PA.

[66] Todd Arbogast. The existence of weak solutions to single porosity and simple dual-porosity models of two-phase incompressible flow. *Nonlinear Analysis: Theory, Methods & Applications*, 19(11):1009 – 1031, 1992. ISSN 0362-546X. doi: https://doi.org/10.1016/0362-546X(92)90121-T.

[67] Mai Bai, Qinggang Ma, and Jean-Claude Roegiers. A nonlinear dual-porosity model. *Applied Mathematical Modelling*, 18(11):602 – 610, 1994. ISSN 0307-904X. doi: https://doi.org/10.1016/0307-904X(94)90318-2.

[68] M. Presho, S. Wo, and V. Ginting. Calibrated dual porosity, dual permeability modeling of fractured reservoirs. *Journal of Petroleum Science and Engineering*, 77(3):326 – 337, 2011. ISSN 0920-4105. doi: https://doi.org/10.1016/j.petrol.2011.04.007.

[69] Bo Guo, Yiheng Tao, Karl Bandilla, and Michael Celia. Vertically integrated dual-porosity and dual-permeability models for co2 sequestration in fractured geological formation. *Energy Procedia*, 114:3343 – 3352, 2017. ISSN 1876-6102. doi: https://doi.org/10.1016/j.egypro.2017.03.1466. 13th International Conference on Greenhouse Gas Control Technologies, GHGT-13, 14-18 November 2016, Lausanne, Switzerland.

[70] K.T. Lim and K. Aziz. Matrix-fracture transfer shape factors for dual-porosity simulators. *Journal of Petroleum Science and Engineering*, 13(3):169 – 178, 1995. ISSN 0920-4105. doi: https://doi.org/10.1016/0920-4105(95)00010-F.

[71] J. Gong and W.R. Rossen. Shape factor for dual-permeability fractured reservoir simulation: Effect of non-uniform flow in 2d fracture network. *Fuel*, 184:81 – 88, 2016. ISSN 0016-2361. doi: https://doi.org/10.1016/j.fuel.2016.06.113.

[72] Robert W. Zimmerman, Teklu Hadgu, and Gudmundur S. Bodvarsson. A new lumped-parameter model for flow in unsaturated dual-porosity media. *Advances in Water Resources*, 19(5):317 – 327, 1996. ISSN 0309-1708. doi: https://doi.org/10.1016/0309-1708(96)00007-3.

[73] Y.-S. Wu and K. Pruess. A multiple-porosity method for simulation of naturally fractured petroleum reservoirs. *Society of Petroleum Engineers*, 3(1):327 – 336, 02 1988. doi: doi:10.2118/15129-PA.

[74] R. G. Baca, R. C. Arnett, and D. W. Langford. Modelling fluid flow in fractured-porous rock masses by finite-element techniques. *International Journal for Numerical Methods in Fluids*, 4(4):337–348, 1984. doi: 10.1002/fld.1650040404.

[75] H. Haegland, A. Assteerawatt, H. K. Dahle, G. T. Eigestad, and R. Helmig. Comparison of cell- and vertex-centered discretization methods for flow in a two-dimensional discrete-fracture–matrix system. *Advances in Water Resources*, 32(12):1740–1755, 12 2009.

[76] M. Karimi-Fard, LJ Durlofsky, and K. Aziz. An efficient discrete-fracture model applicable for general-purpose reservoir simulators. *SPE Journal*, 9(2):227–236, 2004.

[77] Hussein Mustapha, Roussos Dimitrakopoulos, Thomas Graf, and Abbas Firoozabadi. An efficient method for discretizing 3d fractured media for subsurface flow and transport simulations. *International Journal for Numerical Methods in Fluids*, 67(5):651–670, 2011. URL `http://dx.doi.org/10.1002/fld.2383`.

[78] Christophe Geuzaine and Jean-François Remacle. Gmsh: A 3-d finite element mesh generator with built-in pre- and post-processing facilities. *International Journal for Numerical Methods in Engineering*, 79(11):1309–1331, 2009. ISSN 1097-0207. doi: 10.1002/nme.2579.

[79] Mesh classification. `https://www.cfd-online.com/Wiki/Mesh_classification`. Accessed: 2019-05-30.

[80] Guy Bunin. A continuum theory for unstructured mesh generation in two dimensions. *Computer Aided Geometric Design*, 25(1):14 – 40, 2008. ISSN 0167-8396. doi: https://doi.org/10.1016/j.cagd.2007.05.002. URL `http://www.sciencedirect.com/science/article/pii/S0167839607000581`.

[81] Steven J. Owen. A survey of unstructured mesh generation technology. In *INTERNATIONAL MESHING ROUNDTABLE*, pages 239–267, 1998.

[82] Xianhai Meng, Zhongxiang Duan, Qin Yang, and Xing Liang. Local pebi grid generation method for reverse faults. *Computers & Geosciences*, 110:73 – 80, 2018. ISSN 0098-3004. doi: https://doi.org/10.1016/j.cageo.2017.09.012. URL http://www.sciencedirect.com/science/article/pii/S0098300417302765.

[83] Daolun Li, Wenshu Zha, Shufeng Liu, Lei Wang, and Detang Lu. Pressure transient analysis of low permeability reservoir with pseudo threshold pressure gradient. *Journal of Petroleum Science and Engineering*, 147:308 – 316, 2016. ISSN 0920-4105. doi: https://doi.org/10.1016/j.petrol.2016.05.036. URL http://www.sciencedirect.com/science/article/pii/S0920410516302054.

[84] Shahid Manzoor, Michael G. Edwards, Ali H. Dogru, and Tareq M. Al-Shaalan. Interior boundary-aligned unstructured grid generation and cell-centered versus vertex-centered cvd-mpfa performance. *Computational Geosciences*, 22(1):195–230, Feb 2018. ISSN 1573-1499. doi: 10.1007/s10596-017-9686-4. URL https://doi.org/10.1007/s10596-017-9686-4.

[85] Bao Zhu, Jiefu Chen, Wanxie Zhong, and Qing Liu. A hybrid fetd-fdtd method with nonconforming meshes. *Commun. Comput. Phys*, 9:828–842, 03 2011. doi: 10.4208/cicp.230909.140410s.

[86] Verena Hermann, Martin Käser, and Cristóbal E. Castro. Non-conforming hybrid meshes for efficient 2-D wave propagation using the Discontinuous Galerkin Method. *Geophysical Journal International*, 184(2):746–758, 02 2011. ISSN 0956-540X. doi: 10.1111/j.1365-246X.2010.04858.x. URL https://doi.org/10.1111/j.1365-246X.2010.04858.x.

[87] Robert Eymard, Gallouet Thierry, and Raphaèle Herbin. Discretisation of heterogeneous and anisotropic diffusion problems on general non-conforming meshes. sushi: a scheme using stabilisation and hybrid interfaces. *IMA J Numer Anal*, 30, 01 2010.

[88] Richard E. Ewing, Ove Sævareid, and Jian Shen. Discretization schemes on triangular grids. *Computer Methods in Applied Mechanics and Engineering*, 152(1):219 – 238, 1998. ISSN 0045-7825. doi: https://doi.org/10.1016/S0045-7825(97)00191-6. Containing papers presented at the Symposium on Advances in Computational Mechanics.

[89] Sonja Gisinger, Andreas Dörnbrack, and Josef Schröttle. A modified darcy's law. *Theoretical and Computational Fluid Dynamics*, 29(4):343–347, Aug 2015. ISSN 1432-2250. doi: 10.1007/s00162-015-0357-6. URL https://doi.org/10.1007/s00162-015-0357-6.

[90] Douglas N. Arnold. Mixed finite element methods for elliptic problems. *Computer Methods in Applied Mechanics and Engineering*, 82(1):281 – 300, 1990. ISSN 0045-7825. doi: https://doi.org/10.1016/0045-7825(90)90168-L. URL http://www.sciencedirect.com/science/article/pii/004578259090168L. Proceedings of the Workshop on Reliability in Computational Mechanics.

[91] S.D. Connell and P. Stow. The pressure correction method. *Computers & Fluids*, 14 (1):1 – 10, 1986. ISSN 0045-7930. doi: https://doi.org/10.1016/0045-7930(86)90034-4. URL http://www.sciencedirect.com/science/article/pii/0045793086900344.

[92] J. C. Nédélec. A new family of mixed finite elements in r3. *Numerische Mathematik*, 50(1):57–81, Jan 1986. ISSN 0945-3245. doi: 10.1007/BF01389668. URL https://doi.org/10.1007/BF01389668.

[93] D. T. Lee and B. J. Schachter. Two algorithms for constructing a delaunay triangulation. *International Journal of Computer & Information Sciences*, 9(3):219–242, Jun 1980. ISSN 1573-7640. doi: 10.1007/BF00977785. URL https://doi.org/10.1007/BF00977785.

[94] P. L. George and F. Hermeline. Delaunay's mesh of a convex polyhedron in dimension d. application to arbitrary polyhedra. *International Journal for Numerical Methods in Engineering*, 33(5):975–995, 1992. doi: 10.1002/nme.1620330507. URL https://onlinelibrary.wiley.com/doi/abs/10.1002/nme.1620330507.

[95] James M. Ortega. *An introduction to Fortran 90 for scientific computing*. Oxford University Press, 1 edition, 7 1994.

[96] Ian Chivers and Jane Sleightholme. *Introduction to Programming with Fortran: With Coverage of Fortran 90, 95, 2003, 2008 and 77*. Springer Publishing Company, Incorporated, 3rd edition, 2015. ISBN 3319177001, 9783319177007.

[97] Michael Metcalf and John K. Reid. *Fortran 90/95 Explained (2Nd Ed.)*. Oxford University Press, Inc., New York, NY, USA, 1999. ISBN 0-19-850558-2.

[98] Lawrence Livermore National Laboratory: VisIT. https://wci.llnl.gov/simulation/computer-codes/visit/. Accessed: 2019-06-20.

[99] Cong Wang and Yushu Wu. Characterizing hydraulic fractures in shale gas reservoirs using transient pressure tests. *Petroleum*, 1(2):133 – 138, 2015. ISSN 2405-6561. doi: https://doi.org/10.1016/j.petlm.2015.05.002. URL http://www.sciencedirect.com/science/article/pii/S2405656115000164.

[100] Wei Yu and Kamy Sepehrnoori. Chapter 2 - numerical model for shale gas and tight oil simulation. In Wei Yu and Kamy Sepehrnoori, editors, *Shale Gas and Tight Oil Reservoir Simulation*, pages 11 – 70. Gulf Professional Publishing, 2018. ISBN 978-0-12-813868-7. doi: https://doi.org/10.1016/B978-0-12-813868-7.00002-X. URL http://www.sciencedirect.com/science/article/pii/B978012813868700002X.

[101] Ashkan Zolfaghari, Hassan Dehghanpour, Ebrahim Ghanbari, and Doug Bearinger. Fracture characterization using flowback salt-concentration transient. *Society of Petroleum Engineers*, pages 233–244, 2016. doi: 10.2118/168598-PA.

[102] Maziar Arshadi, Arsalan Zolfaghari, Mohammad Piri, Ghaithan A. Al-Muntasheri, and Mohammed Sayed. The effect of deformation on two-phase flow through proppant-packed fractured shale samples: A micro-scale experimental investigation. *Advances in Water Resources*, 105:108 – 131, 2017. ISSN 0309-1708. doi: https://doi.org/10.1016/j.advwatres.2017.04.022. URL http://www.sciencedirect.com/science/article/pii/S0309170816302524.

[103] Julia F. W. Gale, Stephen E. Laubach, Jon E. Olson, Peter Eichhubl, and András Fall. Natural fractures in shale: A review and new observations. *AAPG Bulletin*, 98 (11):2165–2216, 11 2014. ISSN 0149-1423. doi: 10.1306/08121413151. URL https://doi.org/10.1306/08121413151.

[104] Petrophysical properties of shale rocks. https://infolupki.pgi.gov.pl/en/gas/petrophysical-properties-shale-rocks. Accessed: 2019-06-30.

[105] Natural Resources Canada. Geology of shale and tight reservoirs. https://www.nrcan.gc.ca/energy/sources/shale-tight-resources/17675. Accessed: 2019-09-20.

[106] R. G. Santos, W. Loh, A. C. Bannwart, and O. V. Trevisan. An overview of heavy oil properties and its recovery and transportation methods. *Brazilian Journal of Chemical Engineering*, 31(3):571 – 590, 2014.